ISSN 1063-7796, Physics of Particles and Nuclei, 2008, Vol. 39, No. 3, pp. 424–453. © Pleiades Publishing, Ltd., 2008.
Original Russian Text © A.F. Buzulutskov, 2008, published in Fizika Elementarnykh Chastits i Atomnogo Yadra, 2008, Vol. 39, No. 3.

Gaseous Photodetectors with Solid Photocathodes

A. F. Buzulutskov

Budker Institute of Nuclear Physics, Siberian Branch, Russian Academy of Sciences, Novosibirsk, 630090 Russia
e-mail: buzulu@inp.nsk.su

Abstract—Remarkable properties of gas photodetectors make them attractive for application in high energy physics, astrophysics, and medical imaging. This review presents the results of research and development of gaseous photodetectors with solid photocathodes (GPDs). In particular, efficient photocathodes for the ultraviolet (mainly CsI) and the visible ranges, including photocathodes with protective dielectric nanofilms, are described. Some problems of the physics of gaseous photodetectors and photocathodes are considered: photoelectron backscattering in gas, photoemission amplification in an electric field, photoelectron transport through nanofilms, protective properties of nanofilms, and photon and ion feedback. A separate section is devoted to GPDs based on gas electron multipliers (GEMs), including sealed GPDs and cryogenic two-phase avalanche detectors with CsI photocathodes.

PACS numbers: 29.40.Cs; 85.60.Ha

DOI: 10.1134/S1063779608030052

INTRODUCTION

Detectors of photons (photodetectors) are one of the basic types of detectors in high energy and nuclear physics. They are used in fields in which the optical method of signal detection is required, namely, in scintillation counters, Cherenkov counters, ring imaging Cherenkov detectors (RICH detectors), scintillation calorimeters, and so on. The most widespread representatives of photodetectors are vacuum photoelectron multipliers (PMT) and semiconductor photodiodes.

At the same time, gaseous photodetectors sensitive to single photons which use the principle of avalanche amplification in gases (see, e.g., [1, 2]) have been developed for over a quarter of a century. The advantages of gaseous photodetectors when compared to vacuum ones are a large working area, convenient methods for coordinate information readout, and the capability of operating in a magnetic field, and their advantages over semiconductor detectors are a lower noise level and higher gain. As regards such parameters as amplitude and time resolution, they yield to vacuum photodetectors. Thus, the specific field of application of gaseous photodetectors is determined by the tasks in which coordinate photodetectors with relatively large area (more than one square decimeter) are required.

Although photosensitive gaseous counters were known long ago [3–5], the first large-area coordinate gaseous photodetectors were developed in the early 1980s in connection with the development of RICH detectors [1]. They had a gaseous photocathode, i.e., operated using vapors of organic substances with low ionization potential sensitive in the ultraviolet range, such as TEA and TMAE [1]. The field of application of photodetectors with gaseous photocathodes, however, is quite limited for a number of reasons. These reasons are their insensitivity to visible light, incapability of operation at cryogenic temperatures, and impossibility of being used in sealed devices.

Gaseous photodetectors with solid photocathodes in general, and with CsI photocathodes in particular [6], are considered to be more promising. Indeed, the interest in these photodetectors has not decreased in twenty years [2, 7, 8]. The advantages of solid photocathodes are their potential for operation in a wide temperature and pressure range, compatibility with sealed devices, a variety of methods of coupling with amplification structures, and sensitivity in the visible range. Moreover, the advantage of CsI photocathodes which are sensitive in the ultraviolet range is high quantum efficiency in the range of scintillation of noble gases, which can be deployed in liquid scintillation cryogenic detectors [9].

Nonetheless, the application of gaseous photodetectors with solid photocathodes is limited to a few RICH detectors based on CsI photocathodes with gas flow [10] which are in operation or under construction. This is related to the fact that the development of more practical gaseous photodetectors, such as those based on gas electron multipliers [11–14], sealed [15, 16, 20], and with photocathodes for the visible range [17–21], is still topical. If these detectors were developed, they would provide competition for PMT in the fields of traditional application of the latter.

The main obstacle for application in gaseous photodetectors of photocathodes for the visible range is their high chemical activity with respect to oxygen admixtures and water vapors. A possible solution of this problem is the protection of photocathodes by dielectric films with a thickness of several nanometers [22–29], i.e., nanofilms (see, e.g., [30]). In this review, sufficiently large attention is paid to this topic.

Until recently, only multiwire chambers [31] were used as amplification structures in gaseous photodetec-

tors. Further progress in the field of gaseous photodetectors is associated with the application of gas electron multipliers (GEMs) [32–34] and related structures with holes. The unique property of a GEM is the cascading capability, which allows its application in gaseous photodetectors as an amplification structure similar to the dynode cascade in PMT.

The remarkable characteristics of gaseous photodetectors with solid GEM-based photocathodes [11–21] make them attractive for application in high energy physics, astrophysics, and medical imaging. Such applications are, in particular, Cherenkov detectors [35–37] and cryogenic two-phase avalanche detectors [38, 39]. The latter are planned to be used for detection of coherent neutrino scattering off nuclei [40] and dark matter [41, 42], and in positron emission tomography (PET) [43, 44].

In this review, the results of investigation and development of gaseous photodetectors with solid photocathodes are presented. These detectors will be denoted hereinafter by GPDs. In Section 1, the classification and principles of operation of GPDs are considered. Section 2 discusses efficient photocathodes for the ultraviolet and the visible range in gas and vacuum, and dielectric nanofilms on photocathodes are considered in Section 3. Section 4 is devoted to the development of GEM-based GPDs, including sealed GPDs and cryogenic two-phase avalanche detectors with CsI photocathodes.

It should be noted that the physics of gaseous photodetectors and photocathodes is one of the most diverse and complex fields of the physics of radiation detection, and, therefore, is of independent interest. In this review, in particular, such topics as photoelectron backscattering to the photocathode in gas, photoelectron emission amplification in an electric field, photoelectron transport through nanofilms, protective properties of nanofilms, and photon and ion feedback are considered.

1. TYPES AND PRINCIPLES OF OPERATION OF GASEOUS PHOTODETECTORS

Gaseous photodetectors can be classified using several features: with the photocathode for the ultraviolet or the visible range, with semi-transparent or opaque (massive) photocathode, the photocathode based on multiwire chamber or GEM, or operating with gas flow or in the sealed configuration.

Among photocathodes for the ultraviolet range, the most widely spread in the high energy physics is the CsI photocathode [6]. The results of the research performed in the framework of the RD-26 collaboration [45–50] played the decisive role in its successful application. The main result of these investigations was a considerable increase in the CsI photocathode efficiency due to correct choice of the substrate, the heating procedure, and the gas mixture with the lowest photoelectron backscattering effect (see Section 2).

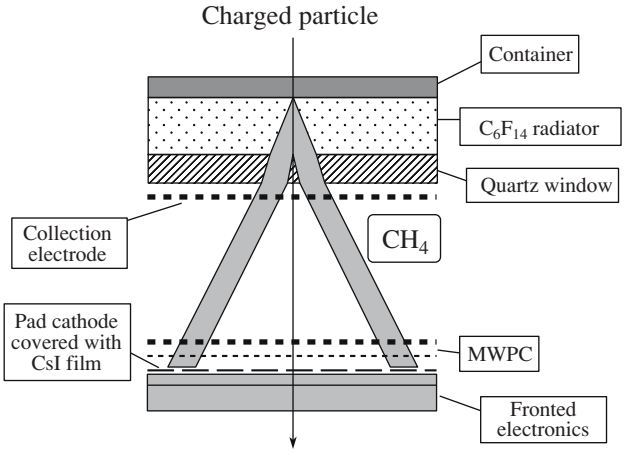

Fig. 1. Schematic diagram of a RICH detector with GPD based on the multiwire chamber and opaque CsI photocathode [51].

Gaseous photodetectors with opaque CsI photocathodes and readout using multiwire chambers are successfully used in the so called proximity focused RICH detectors in experiments at CERN [10, 51], GSI [52], and BNL [10]. Figure 1 shows the schematic diagram of such RICH detector [51]: the Cherenkov radiation emitted in the liquid radiator goes through the quartz window to the multiwire chamber in which it is registered using the CsI photocathode deposited on the cathode areas. The chamber is flushed with pure methane, which provides, first, minimal photoelectron backscattering effect (see Section 2), and second, high (about 5×10^4) gas gain.

Further development of GPDs is associated with the application of GEMs in general [32] and multistage GEMs in particular [11, 13, 14], and related structures with holes, such as capillary plates [53, 54], microhole and strip plates [55], and "thick" GEMs [56, 57]. The "standard" GEM [33, 34] represents the thin dielectric polyamide (Kapton) film with a thickness of 50 μm covered from both sides by the metal (copper) foil with many holes with a diameter of 60–80 μm and a pitch of 140 μm. It is remarkable that first investigations of the three-stage GEM that was most widely spread in track detectors and photodetectors [34] were performed in relation with the development of the gaseous photodetector with the CsI photocathode [11].

Multistage GEMs have a number of advantages necessary for successful operation of GPDs. They are characterized by high gain (above 10^4) in practically any gas mixtures [34], including pure noble [11, 58] and pure molecular [12] gases; suppression of photon [11, 12] and ion [16, 63–65] feedback; capability of coupling with both semitransparent [11] and opaque [13, 14] photocathodes; compatibility with the technique of sealed device production [15, 16, 20]; and efficient operation at

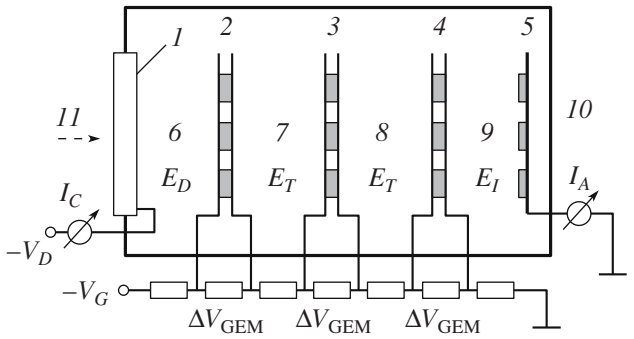

Fig. 2. Schematic diagram of three-stage GEM-based GPD with semitransparent photocathode [11, 16]: *1* is the semitransparent photocathode at the entrance window, *2*, *3*, *4* are the first, second, and third GEMs, *5* is the anode (readout electrode), *6* is the drift gap, *7*, *8* are the transfer gaps, *9* is the induction gap, *10* is the photodetector envelope, *11* is the visible light or ultraviolet radiation, ΔV_{GEM} is the voltage at one GEM, E_D is the drift field, E_T is the transfer field, E_I is the induction field, V_G is the voltage at the divider, V_D is the voltage at the cathode, I_C is the cathode current, and I_A is the anode current.

cryogenic temperatures [38, 59, 60], including in saturated vapors in two-phase systems [39, 59, 61, 62].

As regards the operation principle, GEM-based GPDs can be divided into detectors with semitransparent [11] and opaque [13, 14] photocathodes. The scheme of the GEM-based GPD with the semitransparent photocathode is shown in Fig. 2 [11, 16], and its operation principles are illustrated in Fig. 3. In Fig. 3, physical processes in such a detector [58] are also illustrated; they will be considered in Section 4. The cathode of the photodetector represents the entrance window onto which the semitransparent photosensitive layer is deposited. Photoelectrons generated at the photocathode move in the drift gap along the force lines and are focused in the GEM holes in which electron avalanches develop. Thus, each GEM hole represents an independent proportional counter. A noticeable fraction of avalanche electrons can leave the hole and enter the gas gap for multiplication in subsequent amplification cascades or for detection at the anode (readout) electrode.

The schematic diagram of the GEM-based GPD with the reflective photocathode is shown in Fig. 4 [13, 14]; its difference from the GPD with the semitransparent photocathode is that the entrance window is transparent, the cathode is manufactured in the form of the mesh, and the photocathode is deposited directly on the electrode of the first GEM. The remaining features are similar to those of the scheme shown in Fig. 2. In the case of the GEM-based GPD with the reflective photocathode, one more remarkable GEM property is used: photoelectrons emitted from the first GEM electrode are efficiently collected in the GEM holes for subsequent amplification if the electric field in the drift gap is sufficiently weak (<0.5 kV/cm) [13]. The advantage of this structure is the complete absence of photon feedback to the photocathode and the insensitivity to ionization in the drift gap for zero drift field.

It is these advantages that served as the basis for the development of the original coordinate Cherenkov counter for identification of electron pairs in the experiment PHENIX at RHIC, which realized quite advanced ideas concerning GPDs [35–37]. In this detector, the three-stage GEM and the opaque CsI photocathode deposited on the first GEM are used. The counter is insensitive to hadrons and operates in pure CF_4 without a separating window between the radiator and the photodetector. The latter became possible due to two remarkable properties [12]. First, the GEM-based GPD possesses very high gain in pure CF_4, which allows its operation in the single photon counting mode. Second, it turned out that the CsI quantum efficiency losses due to the photoelectron backscattering are minimal in CF_4 as compared to other gases (see Section 2).

GEM-based GPDs with opaque CsI photocathodes are used in cryogenic two-phase avalanche detectors (Fig. 5). In these detectors [38, 39, 59, 61, 62], primary ionization electrons generated in the noble liquid are emitted into the gaseous phase under the action of the electric field and then amplified using multistage GEMs. In some applications, the signal from primary scintillations in the noble liquid whose spectrum lies in the vacuum ultraviolet range should be registered for suppression of the background in the case of dark matter detection or ensuring fast coincidence between two photons in the case of PET.

It is assumed [34, 39, 61] that the multistage GEM-based GPD with the opaque CsI photocathode deposited on the first GEM can provide efficient detection of both ionization and scintillation signals (Fig. 5). In this case, GEM with the CsI photocathode can be situated in both the gaseous and the liquid phase. In the latter case, it will operate without amplification. The idea of the two-phase Ar avalanche detector with the GEM-based GPD with the opaque CsI photocathode was implemented not long ago [39]. The characteristics of this detector are considered in Section 4.

An interesting method of application of GEM with opaque CsI photocathode was proposed a short time ago for suppression of ion feedback in multistage GEMs [66, 67] on the basis of the so called photoelectric gate (Fig. 6). The gate represents the gap between two neighboring GEMs (or the electroluminescence gap and GEM) at which the potential drop is inverted, blocking the passage of ions from subsequent cascades. The signal transfer through the gate is performed by ultraviolet photons due to secondary scintillations in the noble gas in the first GEM (or the electroluminescence gap) and the photoelectric emission from the second GEM coated with the CsI photocathode. In this way, the ion feedback can be suppressed completely.

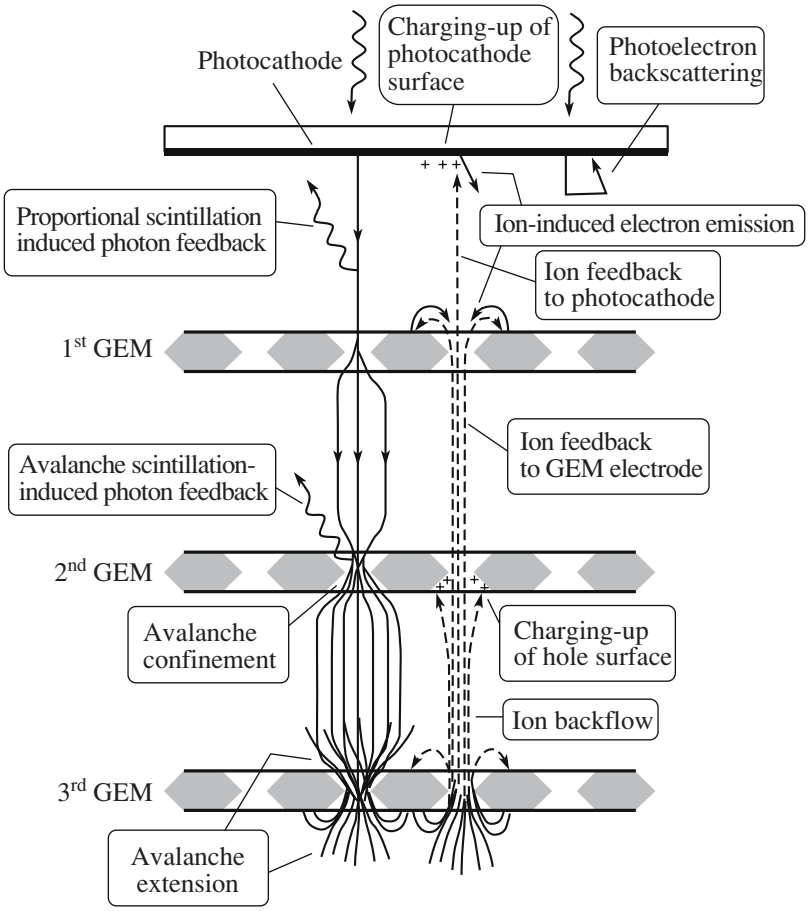

Fig. 3. Principles of operation and physical processes in multistage GEM-based GPG with semitransparent photocathode [58, 34].

Gaseous photodetectors with photocathodes for the visible range and sealed GPDs are in development at present; they are considered in more detail in Section 4.

2. EFFICIENT PHOTOCATHODES FOR GASEOUS PHOTODETECTORS

2.1. Types of Photocathodes

A detailed description of photocathodes used in vacuum devices can be found, e.g., in [68]. In this review, we consider only those photocathodes which were studied in relation with the application in gaseous photodetectors. In this section, only reflective photocathodes are considered.

Solid photocathodes for gaseous photodetectors can be divided into groups according to the production method, chemical composition, and chemical activity with respect to ambient air. The first group includes photocathodes produced using the method of vacuum evaporation, these are alkali halide CsI [6], NaI [45], CsBr [69], and CuI [45] photocathodes. They are sensitive in the ultraviolet range and can be relatively stable in ambient air for approximately half an hour, which considerably simplifies the procedure of gaseous pho-

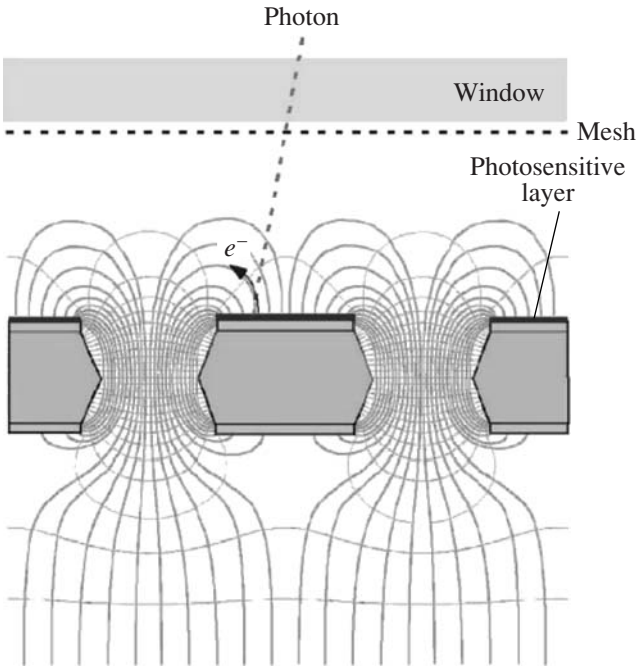

Fig. 4. Principle of operation of GPD with reflective photocathode deposited on GEM [14]. The electric field pattern in the neighborhood of GEM holes is shown.

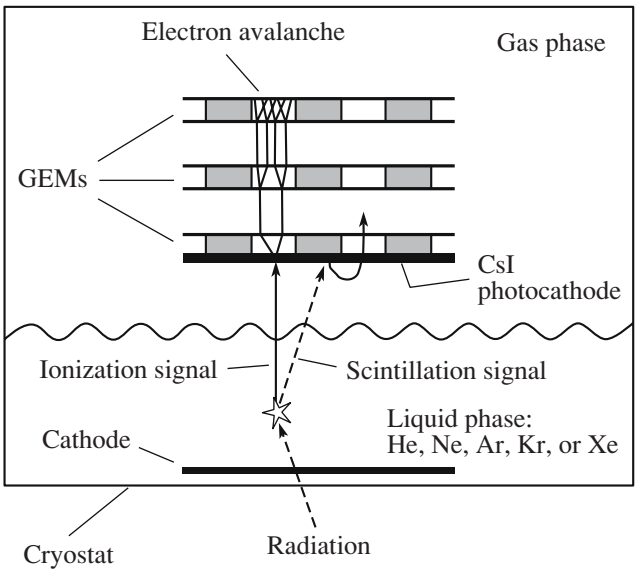

Fig. 5. Principles of operation of the two-phase avalanche detector with a multistage GEM-based GPD with opaque CsI photocathode deposited on the first GEM [34, 39]. Both the scintillation and the ionization signals are registered using the GEMs.

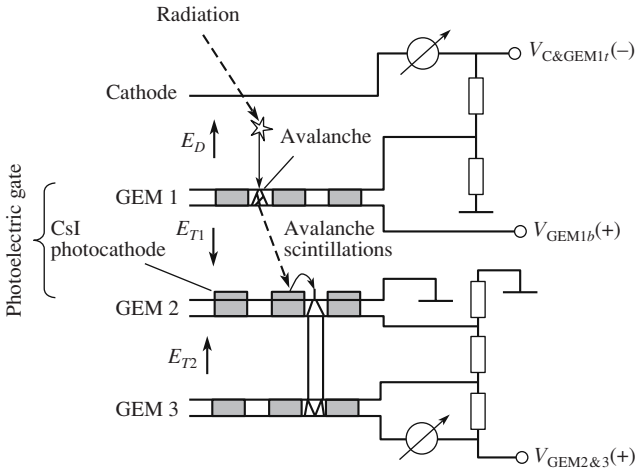

Fig. 6. Multistage GEMs with the photoelectric gate based on opaque CsI photocathode deposited on the second GEM [66]. The photoelectric gate suppresses the ion feedback due to electric field inversion between the first and the second GEMs.

todetector assembling. The group of photocathodes operating in the ultraviolet range that are stable in air also includes photocathodes based on diamond-like films produced using the method of chemical vapor deposition [70].

Another group is formed by photocathodes for the visible and near ultraviolet range produced using the method of activation by vapors of alkali metal; these are the cesium–antimony (Cs–Sb) [17], the bi-alkali (Cs–K–Sb) [17], and the tellurium–cesium (Cs–Te) [71] photocathodes. Due to high chemical activity, these photocathodes cannot be transported in air. Therefore, they are mounted using the method of vacuum transportation [17], which complicates considerably the assembling of the gaseous photodetector [20].

2.2. Efficient Photocathodes for Ultraviolet Range

Among photocathodes for the ultraviolet range that are relatively stable in air, CsI has the highest efficiency. This can be seen in Fig. 7, in which the spectra of the quantum efficiency for opaque CsI, NaI, CuI, CsBr, and diamond-like photocathodes in vacuum are shown. This is probably related, among other reasons, with the fact that CsI has sufficiently small electron affinity, $E_A = 0.1$–0.2 eV, for the width of the forbidden zone $E_G = 5.9$–6.0 eV [23]. Therefore, a major part of research concerning ultraviolet photocathodes is devoted to CsI photocathodes. At the same time, complete understanding of some of its properties is still lacking. The history of the problem and the status of this topic are presented in comprehensive review [6].

The following works are the key ones in investigation of the properties of the CsI photocathode. In [72, 73], quantum efficiencies for opaque alkali halide photocathodes in vacuum were measured systematically; it became clear from these measurements that CsI has the largest quantum efficiency. In [74], the possibility of coupling the CsI photocathode with the gaseous wire chamber was demonstrated. In [75], it was shown that the quantum efficiency of the opaque CsI photocathode can be sufficiently high not only in vacuum, but also in such gases as methane. In [76], characteristics of the

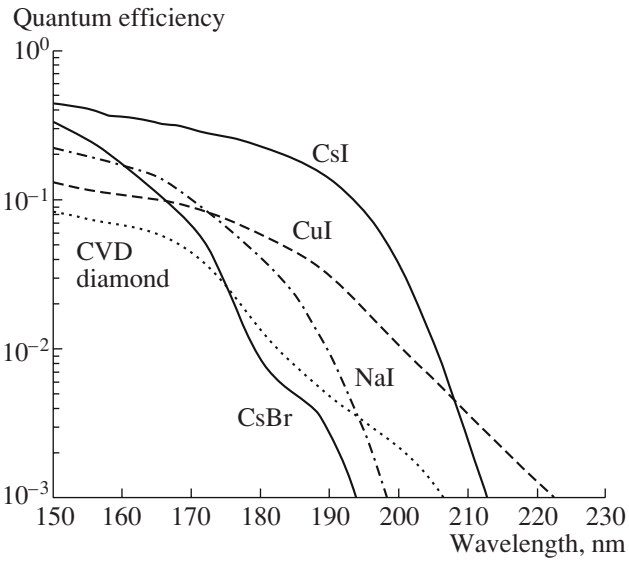

Fig. 7. Quantum efficiency spectra for opaque ultraviolet photocathodes in vacuum: CsI [45], CsBr [2], NaI [45], CuI [45] (after heat treatment) and the diamond-like photocathode [2].

semitransparent CsI photocathode were studied in detail. In [77], it was shown using calibrated photoreceptors that the absolute quantum efficiency of the opaque CsI photocathode is indeed very high, reaching 20% for 185 nm and more than 40% for 150 nm (Fig. 7).

It was shown in [78, 79] that the decisive factor in obtaining a high quantum efficiency for the CsI photocathode is the procedure of heat treatment after evaporation, and in [45] it was proved that this procedure has a universal character, i.e., is applicable to other ultraviolet photocathodes as well. The application of this procedure for mass production of CsI photocathodes is described in [80]. In [50], it was shown that the role of the substrate can also be significant.

The problem of photoelectron backscattering to the photocathode, which results in the decrease in CsI quantum efficiency in gas as compared to vacuum, is closely related with the electric field effect; this problem was solved in a series of works [46–48]. The effect of enhancement of photoelectron emission from CsI in strong electric field in vacuum was observed in [81].

In [82], the electric resistance of film CsI photocathodes was measured. In [6], processes of CsI photocathode aging under the action of humid air, photons, and ions studied earlier in a number of works were systematized.

It was shown in [83] that CsI efficiency in cryogenic liquids Ar, Kr, and Xe can be comparable with the efficiency in vacuum. It was shown in [84] that the CsI photocathode does not lose efficiency at cryogenic temperatures in gases, and in [39] that it can operate in saturated vapors in two-phase Ar.

Let us consider the methods of producing efficient CsI photocathodes. The typical procedure of production of the opaque CsI photocathode includes the vacuum evaporation to the substrate of the CsI film with a thickness of about 0.5 μm and substrate heating for several hours [23]. The evaporation is performed in high vacuum (10^{-5}–10^{-8} Torr) at a temperature on the order of 600°C from a tantalum or a molybdenum boat by its heating with the help of large electric current (of order of several tens of ampere) or an electron beam. Printed circuit boards from which wire chamber cathodes and GEM electrodes are made can be used as the substrate. It is necessary, however, to avoid direct contact of CsI with copper from which the circuit boards are made due to CsI dissociation on copper [50]. For this reason, circuit boards are coated with additional Ni/Au layers [6, 50].

The problem of increasing the efficiency of the CsI photocathode using heat treatment plays a special role; it was noted that this processing is the key factor for achieving and stabilizing high quantum efficiency [45, 50, 78, 79]. In this case, the quantum efficiency in the long-wavelength range can be increased by several orders of magnitude (Fig. 8). It turned out that heat treatment influences positively other photocathodes along with CsI, the iodides NaI [45], CuI [45], and KI [85], and the bromide CsBr [69] (see Fig. 8). Thus, the general tendency for ultraviolet photocathodes produced using the method of vacuum evaporation can be noted.

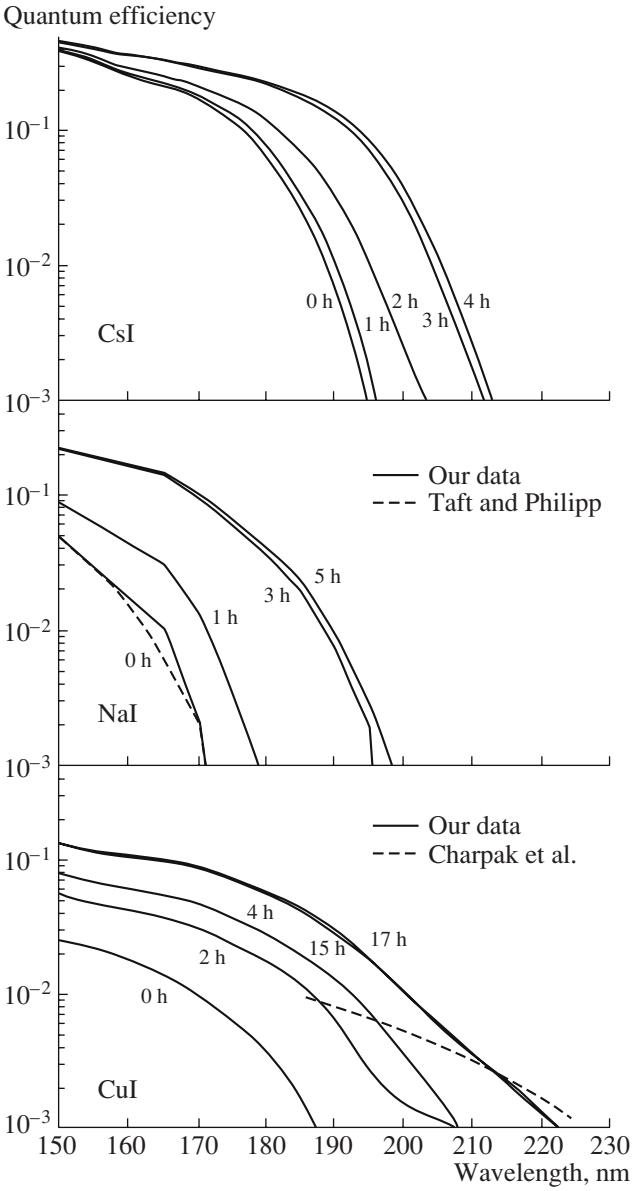

Fig. 8. Quantum efficiency amplification for CsI, NaI, and CuI photocathodes achieved by heat treatment in vacuum after evaporation to the substrate. The evolution of the spectra of the quantum efficiency of the following reflective photocathode in vacuum is shown: CsI after heating for 0, 1, 2, 3, and 15 h at 60°C [79], NaI after heating for 0, 1, 3, and 5 h at 70°C [45], and CuI after heating for 0, 2, 4, 15, and 17 h at 70°C [45]. Dashed line shows data for NaI and CuI from [72] and [86], respectively.

Heat treatment is usually performed in vacuum. A temperature of 50–70°C and a time period of several hours, after which the quantum efficiency is saturated [45, 79], are sufficient for this processing. Heating at higher temperature (165°C) does not result in a further increase in efficiency [45].

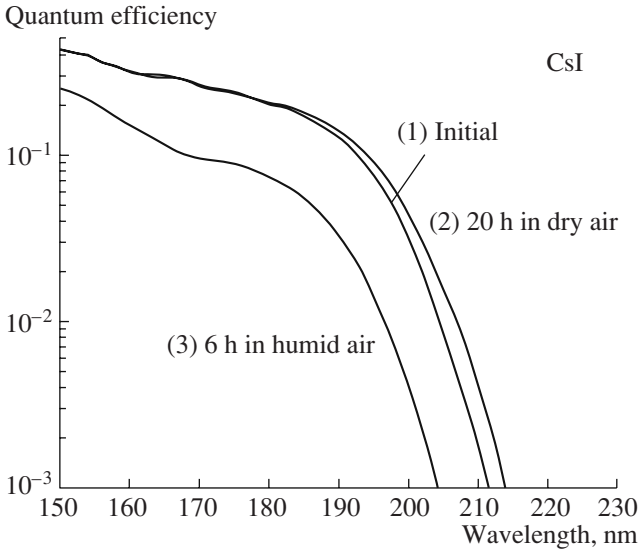

Fig. 9. Evolution of the quantum efficiency spectrum for the opaque CsI photocathode: (*1*) after heat treatment, (*2*) after exposure in dry air for 20 h, and (*3*) after exposure in humid air with a relative humidity of 60–70% for 6 h [22].

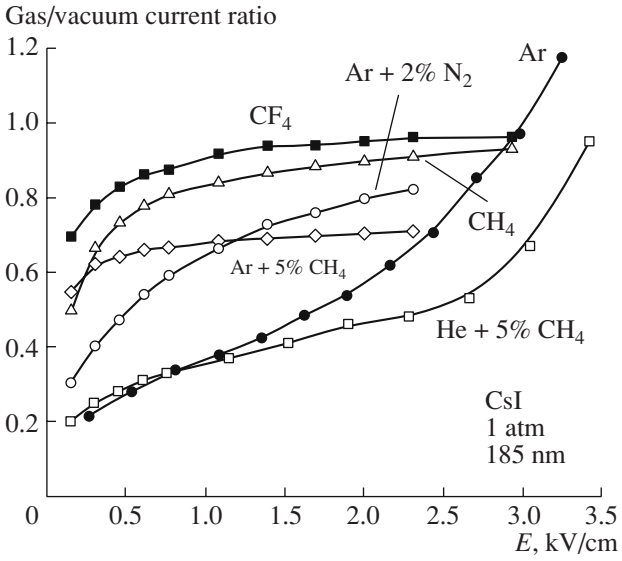

Fig. 10. Photoelectron backscattering to the opaque CsI photocathode in different gases at atmospheric pressure [11, 12, 47]. The ratio of photocurrents in gas and vacuum for a wavelength of 185 nm as a function of the electric field strength at the photocathode is shown.

The universal character of heat treatment resulted in the essential reconsideration of quantum efficiencies and values of electron affinity for ultraviolet photocathodes [45]. In particular, this is seen from the comparison of the NaI spectra in Fig. 8. While the spectrum of the photocathode before heat treatment [45] practically coincides with the spectrum presented earlier in other works [72], after heat treatment, the photocathode efficiency is increased more than several times, and the long-wavelength boundary of the spectrum is shifted by ~ 1 eV. The quantum efficiency spectra of most studied ultraviolet photocathodes that were thermally processed are shown in Fig. 7.

It should be noted that the understanding of the mechanism of action of heat treatment is still lacking. At the same time, the universal character of this phenomenon helps to reduce the number of possible explanations. For example, the hypotheses of activation of the photocathode surface due to the increased content of cesium and the restructuring of the crystal lattice can be excluded [45]. The hypothesis in which the efficiency is increased due to removal of water vapors from the photocathode as a result of heating is also incapable of explaining everything (this hypothesis is considered as the basic one in [80]). Indeed, the action of heat treatment on NaI and CuI is practically similar (see Fig. 8) in spite of the fact that their solubility in water differs by five orders of magnitude. One possible explanation can be the effect of stoichiometry variation on the photocathode surface due to the excess of iodine or bromine formed in the course of evaporation. As a result, compounds of the CsI_3 or CsI_5 type which are easily volatilized or decomposed at increased temperature can be formed on the surface [45].

CsI photocathodes are stable in dry air, but can lose efficiency under the action of humidity; in this case, thermally processed photocathodes are more stable [6]. This is seen, in particular, in Fig. 9, which shows the evolution of the quantum efficiency after the photocathode was placed in dry and humid air [22]. In moderately humid air (with a humidity of 50%), practically no loss in efficiency is observed over 15–30 min [50]. This time is quite sufficient for mounting the photocathode into the photodetector.

Aging of photocathodes in GPDs under the conditions of gas amplification is considered in Section 4.

2.3. Effect of Photoelectron Backscattering to CsI Photocathode in Gas

One of the most characteristic properties of GPD is the effect of photoelectron backscattering; the essence of this effect is that some fraction of photoelectrons emitted from the photocathode are diffused back to the cathode as a result of elastic collisions with gas molecules even in the presence of electric field [87]. In the general case, this effect results in a noticeable decrease in the photocathode quantum efficiency in gas as compared to vacuum [11, 12, 46, 47].

This is seen, in particular, from Fig. 10, which shows the ratio of photocurrents for the CsI photocathode in gas and vacuum for different gas mixtures at atmospheric pressure as a function of electric field strength. The effect of photoelectron backscattering is the strongest in monatomic noble gases, since in these

gases the contribution of the elastic channel into scattering is much larger than in molecular gases [87]. For example, for a field of 1 kV/cm, the photocathode efficiency in Ar is less than 40% of the efficiency in vacuum [11, 47]. At the same time, there exist molecular gases and mixtures in which the photocathode quantum efficiency can make up more than 90% of that in vacuum; these are, first of all, CF_4 [12] and CH_4 [11, 46, 47] (see Figs. 10 and 11). It can be seen from Fig. 10 that Ar mixtures with the addition of N_2, in which the photocathode efficiency can reach 80% of that in vacuum for a field of 2 kV/cm [11, 12], can also be related to such mixtures.

The CsI photocathode in C_2H_6 and i-C_4H_{10} [46] has approximately the same efficiency, about 80% of the vacuum efficiency (see Fig. 11). Thus, "good" gases for minimization of the effect of photoelectron backscattering are CF_4 and CH_4, "moderately good" gases are C_2H_6, i-C_4H_{10}, Ar + N_2, and Ar + CH_4, and "bad" gases are pure noble gases and He-based mixtures. It is this property that was taken into account when CF_4 and CH_4 were chosen as the gases for photodetectors with CsI photocathode for RICH detectors in the experiments PHENIX [35] and ALICE [51], respectively.

The photoelectron backscattering, probably, weakly depends on pressure (compare Figs. 10 and 11), but obviously can depend on the photoelectron energy and, therefore, on the wavelength of incident radiation. This can be seen from Fig. 11; for wavelengths in the range 175–190 nm, the photocathode quantum efficiency in gas weakly depends on the wavelength. At the same time, for longer waves and possibly for shorter waves, the photocathode efficiency in gas is decreased even in methane; i.e., here, the photoelectron backscattering begins to play its role. For a wavelength of 170 nm, methane and ethane are still transparent for near ultraviolet radiation, and isobutane already begins to absorb radiation. Probably, this explains stronger decrease in efficiency in isobutane observed in the short-wavelength region. It is interesting that the enhancement of photoelectron backscattering with decreasing wavelength, which is possibly observed in experiment (see Fig. 11), is also predicted in [88], where this effect is simulated numerically.

There exists another method of increasing the efficiency of photocathodes in gas due to the suppression of photoelectron backscattering; this method is applicable to any gas. The essence of this method is the suppression of elastic scattering of photoelectrons due to an increased contribution of inelastic channels: this is achieved by a transition to the gas amplification mode in the gap containing the photocathode [46]. This effect was first observed at low pressures [46] and then was studied at atmospheric pressure [47, 48].

The relative quantum efficiency of a CsI photocathode measured using the photon counting technique is shown in Fig. 12 as a function of the electric field strength in ethane and in the mixture He + 5% CH_4 at

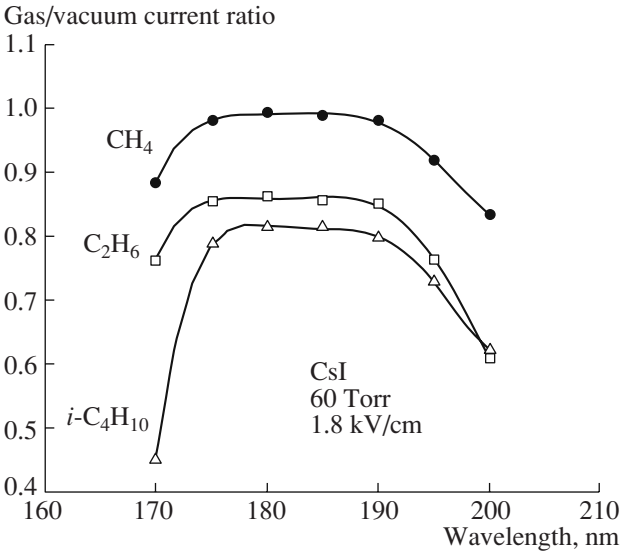

Fig. 11. Photoelectron backscattering to opaque CsI photocathode in methane, ethane, and isobutane at pressure of 60 Torr [46]. The ratio of photocurrents in gas and vacuum as a function of the wavelength at an electric field strength at the photocathode of 1.8 kV/cm is shown.

low and high pressure, respectively. Also shown is the gas amplification as a function of the field strength. The characteristic quantum efficiency correlated with the operation mode for the gas gap is observed: the quantum efficiency reaches the plateau two times. The first yield plateau corresponds to the ionization mode, and then, in the course of transition into the gas amplification mode, the quantum efficiency rises again and reaches the plateau for the second time, now with amplification larger than 100. Similar behavior has been observed in other gases as well [46–48]. It is characteristic that the difference in the quantum efficiency for the first and the second plateau corresponds to the difference in the quantum efficiency in gas and vacuum measured in the current mode. This evidently means that the photocathode efficiency in gaseous medium in the gas amplification mode is equal to the efficiency in vacuum; i.e., the photoelectron backscattering effect here turns out to be completely suppressed.

Although this method of increasing the photocathode efficiency has not been used in practice, it can be used for photodetectors working in pure noble gases. It should be noted, however, that the operation of the cathode gap in the gas amplification mode has negative consequences due to the ion feedback to the cathode, which can limit both the photocathode lifetime and the maximum GPD amplification; this especially applies to the visible range [20] (see Section 4).

Nonetheless, this problem, probably, has a solution. Simulation shows [89] that for suppressing photoelectron backscattering, it is not necessary to pass to the gas amplification mode. In pure Ar, it is sufficient to change over to the mode of inelastic collisions at which no ion

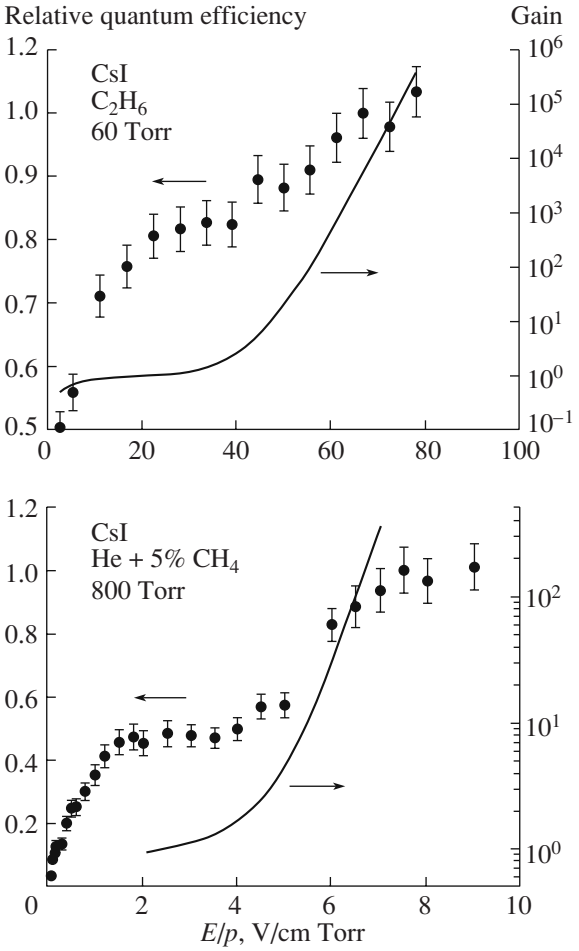

Fig. 12. Suppression of the photoelectron backscattering in the gas amplification mode. The relative quantum efficiency of opaque CsI photocathode at a wavelength of about 190 nm measured using the photon counting method and the gas amplification in the cathode gap as functions of the electric field strength at the photocathode in ethane at 60 Torr [46] and He + 5% CH_4 mixture at 800 Torr [47] are shown.

feedback is formed. Calculations show that the CsI photocathode efficiency in this case rises up to 80% from the efficiency in vacuum for a field strength of about 2.5–3 kV/cm [89]. Partially, this can explain the increase in the ratio of photocurrents in Ar and vacuum in Fig. 10 for fields higher than 2 kV/cm.

2.4. Enhancement of Photoelectron Emission from CsI in Strong Electric Field

In the previous section, the influence of the electric field on the quantum efficiency of the CsI photocathode in gas environment at relatively low field strengths (smaller than 10 kV/cm) was considered; under these conditions, the main effect is the photoelectron backscattering on gas molecules. In this section, emission properties of CsI in strong electric fields reaching 500 kV/cm [81] are described.

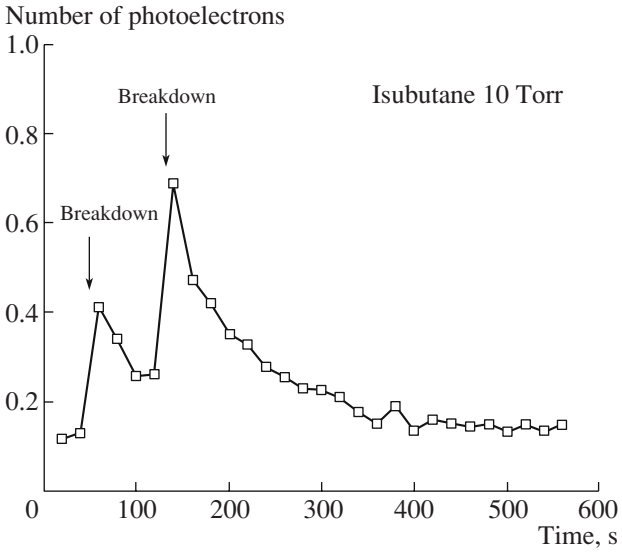

Fig. 13. Enhancement of photoelectron emission from an opaque CsI photocathode after breakdowns in the wire chamber in isobutane at a pressure of 10 Torr [46]. The number of photoelectrons emitted from CsI per one light pulse of the hydrogen lamp as a function of time is shown.

These investigations were initiated by observations in which the quantum efficiency of the CsI photocathode in gas was increased several times after breakdowns [46] (see Fig. 13). This occurred, probably, due to the local increase in the positive charge density on the CsI surface. Since CsI is a dielectric, positive ions cannot be neutralized promptly, which may result in the creation of a strong electric field on the surface reaching several hundreds of kV/cm. It was assumed [46] that it is this field that is the reason for enhancement of photoelectron emission due to the decreased work function of CsI, similar to the Schottky effect in metals.

In experiments on photoelectron emission in a strong electric field, the wire photocathode coated with the CsI film placed between two anode plates was used. The photocurrent from the wire cathode in vacuum was measured. The dependence of the relative quantum efficiency of CsI on electric field strength on the surface of the wire photocathode measured in this way is shown in Fig. 14 [81]. It can be seen that the effect of enhancement of photoelectron emission under the action of the electric field is quite considerable and increases with increasing wavelength: for a field of 500 kV/cm, the gain factor is 1.5 for 160 nm, 3 for 185 nm, and about 25 for wavelengths larger than 200 nm.

The effect of enhancement of photoelectron emission under the action of a strong electric field was used for enhancement of the response of the CsI photocathode to scintillation of $KMgF_3$ and BaF_2 crystals [90] which emit, respectively, in the vacuum ultraviolet and the ultraviolet range: $KMgF_3$ in the range 140–190 nm [91] and BaF_2 in the range 180–240 nm (fast component) [92]. The most promising is the BaF_2 scintillator, since

it has sufficiently high density and atomic number, which is important for applications in fast calorimetry in high energy physics and PET.

The photodetector should be insensitive to the slow component of BaF_2 scintillation, i.e., wavelengths larger than 250 nm [92]. The ideal solution would be the application of photodetectors with the CsI photocathode, since its red boundary is 210 nm. At the same time, the overlapping of the radiation spectra of BaF_2 and the quantum efficiency for CsI is clearly insufficient [93], for example, for application in PET. Therefore, the possibility of enhancement of CsI response to scintillation of BaF_2 using a strong electric field seems attractive.

This possibility was realized in [90]: the wire CsI photocathode was attached to $KMgF_3$ and BaF_2 scintillators irradiated by an intense source of γ rays. The response amplification factor for BaF_2 turned out to be considerably larger than for $KMgF_3$: for a field of 400 kV/cm, it was 3 and 1.5, respectively. This is in agreement with data on enhancement of photoelectron emission at 160 and 185 nm (Fig. 14), which correspond to the convolution of the radiation spectra of $KMgF_3$ and BaF_2 and the quantum efficiency of CsI.

It should be noted, however, that although several variants of practical application of the effect of strong electric field in gas and vacuum photodetectors were proposed [79, 81], it would be difficult to implement them.

It is assumed that photoelectron emission is enhanced mainly due to the decreased work function of the photocathode under the action of electric field as a result of the Schottky effect. In this case, the affinity to the electron in the electric field is decreased by [81]

$$\Delta E_a = e(\alpha eF)^{1/2},$$

$$\alpha = (\varepsilon_\infty - 1)/(\varepsilon_\infty + 1).$$

Here, e is the electron charge, F is the electric field strength, and ε_∞ is the radiofrequency dielectric permeability of CsI. A simple model based on this assumption describes well the dependence of CsI quantum efficiency on electric field strength [81]. In a more complex microscopic model taking into account the electron transport in CsI, the leading role of the effect of decreasing the vertical potential barrier on the surface in the strong electric field was also shown [94].

In conclusion to this section, it should be mentioned that the strong electric field, along with the photoelectron emission, efficiently amplifies the secondary electron emission from CsI as well [81].

2.5. Efficient Photocathodes for the Visible Range

The procedure of production of efficient photocathodes for the visible range is not only more complicated, but also must be performed in cleaner conditions at higher vacuum than for ultraviolet photocathodes considered above. Therefore, photocathodes for the visible range intended for application in GPD were studied only at two laboratories that possess the appropriate equipment [17, 20, 25, 26, 54, 95].

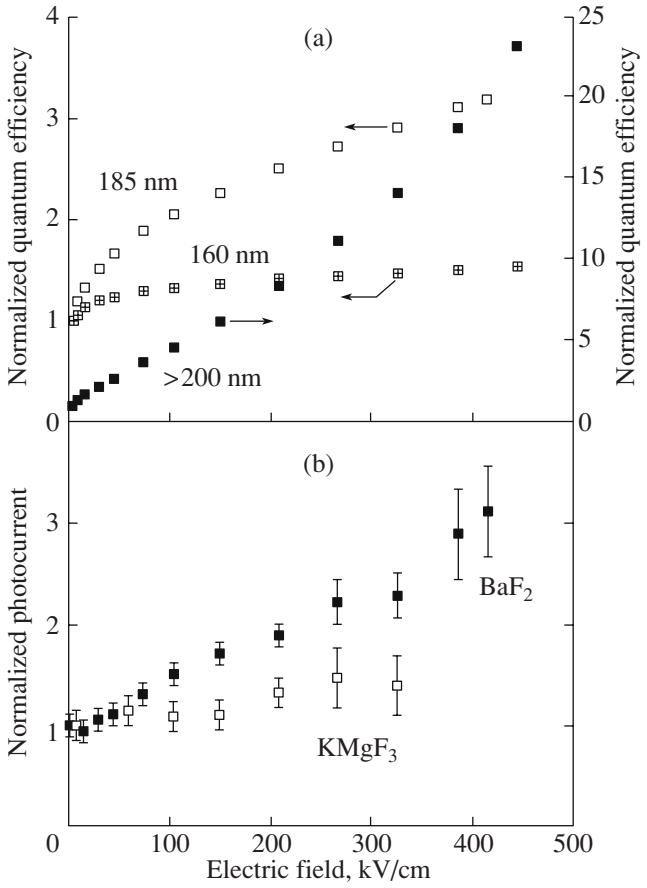

Fig. 14. Effect of strong electric field. (a) Relative quantum efficiency from opaque CsI photocathode in vacuum at wavelengths of 160, 185, and larger than 200 nm [81]; (b) relative photocurrent from the CsI photocathode for $KMgF_3$ and BaF_2 scintillators irradiated by γ rays as a function of electric field strength [90].

In particular, Fig. 15 shows the unique setup developed at the Weizmann Institute for production and investigation of the properties of alkali–antimony photocathodes for the visible range and for deposition of protective films on these photocathodes [17]. The specific feature of the setup is that the photocathode can move inside the vacuum chamber between three positions: for production of the photocathode, for deposition of protective films, and for measurement of the quantum efficiency. The photocathode production including the operations of antimony evaporation and activation by alkali metals was performed in a closed glass cylinder with a heater. The chamber could also be filled with different gases for the investigation of the photocathode stability and the protective properties of films in gaseous medium.

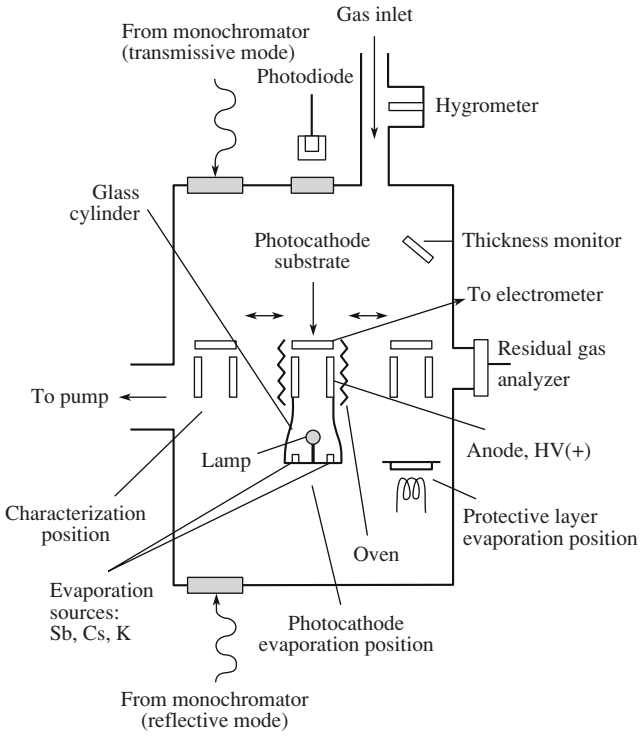

Fig. 15. Experimental setup for production and investigation of photocathodes for the visible range and deposition of protective films on them [17].

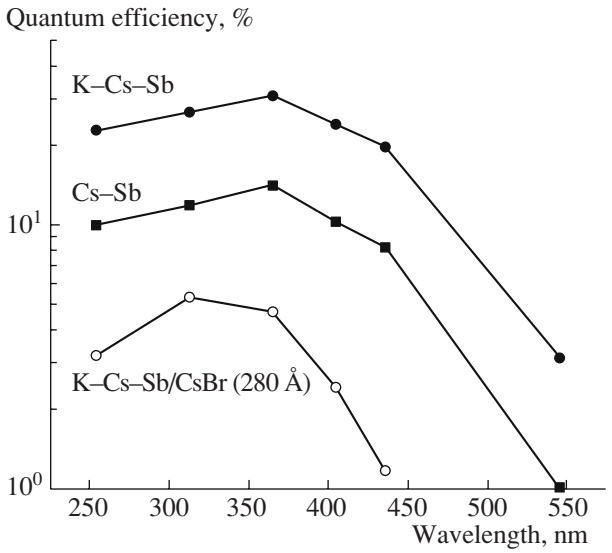

Fig. 16. Spectra of quantum efficiency for reflective photocathodes for the visible range in vacuum: cesium–antimony (Cs–Sb) photocathode [25], bi-alkali (K–Cs–Sb) cathode [17], and bi-alkali cathode coated with CsBr film with a thickness of 280 Å (K–Cs–Sb/CsBr (280 Å)) [26]. Data of cited papers were refined and reprocessed.

Two types of alkali–antimony photocathodes were studied at this setup: the cesium–antimony (Cs–Sb) and the bi-alkali (K–Cs–Sb) photocathodes. The typical procedure of photocathode production consisted of several stages. At the first stage, common to both types, an antimony layer with a thickness corresponding to a decrease of the substrate transparency to 70% of the initial value was evaporated on the quartz substrate. In the case of the Cs–Sb photocathode, the second stage consisted in activation of the substrate by cesium vapors at 160–170°C; evaporation of cesium was terminated when the photocurrent, which was measured continuously during the process, reached its maximum. In the case of the K–Cs–Sb photocathode, the procedure was more complex: the substrate with the antimony layer was first activated by potassium vapors at 190–200°C up to the photocurrent saturation, and then was promptly heated to 240°C for removing excessive potassium and cooled to 160–170°C. At this temperature, the final stage of activation took place; this final stage consisted in consecutively repeated cesium and antimony evaporation until the maximum photocurrent was reached.

The spectra of the quantum efficiencies for typical opaque Cs–Sb [25] and K–Cs–Sb [17] photocathodes obtained using this procedure are shown in Fig. 16. It can be seen that the quantum efficiency of Cs–Sb and K–Cs–Sb photocathodes is sufficiently high and reaches a maximum of 15 and 30%, respectively. The photocathodes behaved stably; their efficiency did not change at storage both in vacuum and in pure methane [24, 17].

The alternative methods of production of Cs–Sb and K–Cs–Sb photocathodes (with lower efficiency, however) for application in GPD are described in [54, 95].

3. DIELECTRIC NANOFILMS ON PHOTOCATHODES FOR THE ULTRAVIOLET AND VISIBLE RANGES

3.1. Photocathodes with Dielectric Nanofilms for the Ultraviolet and Visible Ranges

It is well known that photocathodes for the visible range, in particular, alkali–antimony photocathodes, are chemically active with respect to air, or more specifically, oxygen admixtures and water vapors. This is the main obstacle for their application in GPD. It should hardly be expected that photocathodes for the visible range which are stable in air will be found in near future.

As a consequence, several groups independently proposed the following idea for protection of photocathodes using thin films [76, 96, 97]. The essence of this idea is that a dielectric film is deposited on the photocathode using the method of vacuum evaporation; the thickness of this film is several nanometers; i.e., it is a nanofilm. A nanofilm is an ultrathin film with a thickness up to 100 nm or 1000 Å [30]. This nanofilm, on the one hand, should protect the photocathode from harmful admixtures in gas, while, on the other hand, not impeding photoelectron emission, i.e., photoelectron transport, through it. Obviously, for the second condition to be satisfied, the nanofilm should be, first of all,

chemically inert with respect to the photocathode. Moreover, it should not form a high potential barrier at the interface with the photocathode, and the escape length in it should be sufficiently large, at least on the order of its thickness.

The first attempts at deposition of protective films to photocathodes for the visible range turned out to be not very successful, since their protective properties with respect to air were unsatisfactory and the quantum efficiency of covered photocathodes did not exceed fractions of a percent, which made them inapplicable for practical use [96, 97]. Nonetheless, it was shown in [97] that the CsI film is a good candidate for a protective film, since it turned out to be chemically inert with respect to the Cs–Sb photocathode.

The photoelectron transport through different dielectric nanofilms was systematically studied first for CsI [23] and then for Cs–Sb and K–Cs–Sb photocathodes [25–27, 98]. As a result, several types of nanofilms with the largest photoelectron escape length were chosen. They are, first of all, CsBr, CsI, and NaI, and some other organic films. An interesting property of organic films is that it is possible to remove them from the photocathode by heating [29] (see Section 3.3).

The protection of alkali–antimony photocathodes from oxygen was first demonstrated by the example of NaI film [24]. Further, it was discovered that CsBr [26] and CsI [25, 27] nanofilms also provide efficient protection and high quantum efficiency (reaching 5%) for Cs–Sb and K–Cs–Sb photocathodes.

Nanofilms are applied to the photocathode after its production using the method of vacuum evaporation at setups similar to that shown in Fig. 15. The film thickness is determined using a measurement of quartz sensor oscillation frequency. The conditions of obtaining a certain film, in particular, the deposition rate, the substrate temperature, heat treatment, etc., are described in detail in [23] for CsI photocathodes and in [25, 26] for alkali–antimony photocathodes.

Let us consider the CsI photocathode with the LiF film as an example. Figure 17 shows the microphotos of the surface of the CsI photocathode before and after the application of the nanofilm [23]. In the initial state, the CsI surface shows a pronounced polycrystalline structure. After a LiF nanofilm with a thickness of 20 Å is deposited on the CsI surface, this structure becomes completely unobservable. This testifies that even such an ultrathin film is continuous, which is very important for its capability to protect the photocathode and for investigation of its transport characteristics.

Figure 18 shows the diagram of energy zones at the CsI–LiF–vacuum interface [23]. The process of photoelectron emission in this system consists of absorption of the photon in the photocathode, transition of the photoelectron from the valence zone to the conductivity zone, transport of the photoelectron through the photocathode and the dielectric film, and emission into vacuum through the potential barrier at the vacuum boundary. In the general case, the deposition of the dielectric film to the photocathode results in the weaker photoelectron emission due to quasielastic and inelastic collisions of the photoelectrons with acoustic and optical phonons in the film (see, e.g., [94]) and scattering on defects. Besides, an increase or decrease in the height of the potential barrier at the surface is possible, which leads to the additional attenuation or enhancement of emission.

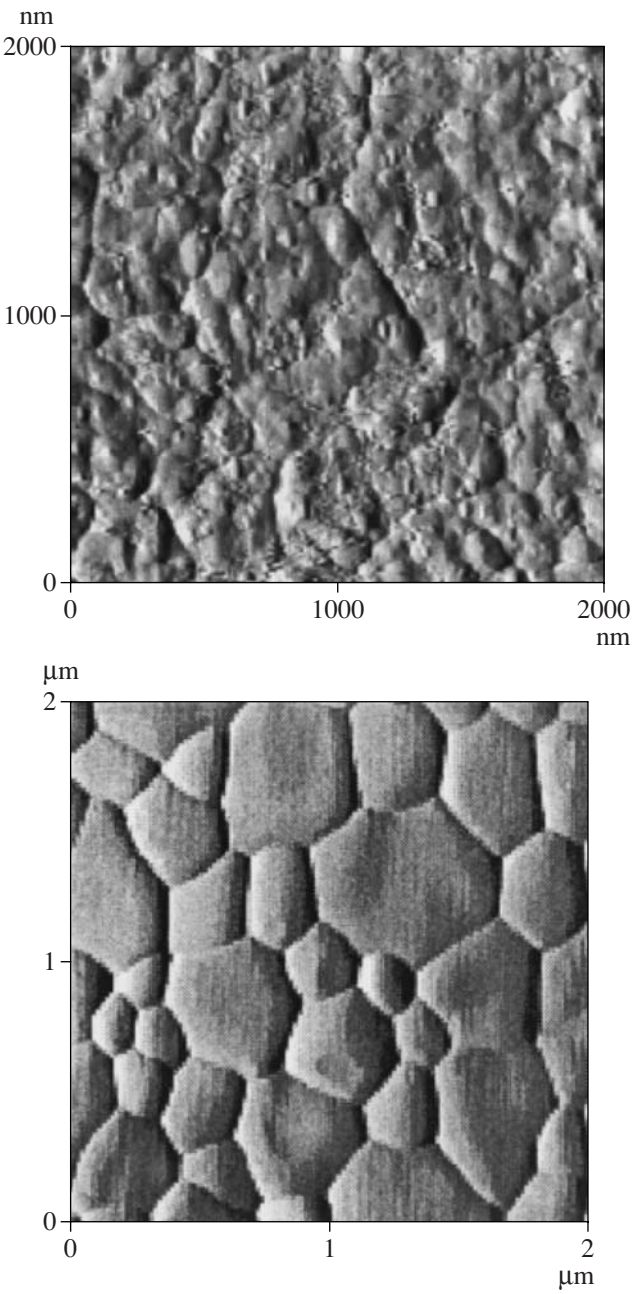

Fig. 17. Microphotos of the surface of CsI photocathode (lower figure) before and (upper figure) after coating with the LiF nanofilm with a thickness of 20 Å obtained using the atomic force microscope [23].

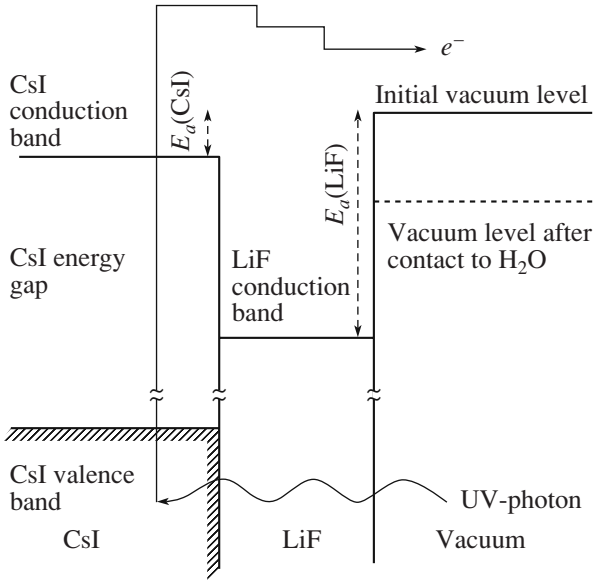

Fig. 18. Simplified diagram of energy zones for CsI photocathode coated with LiF film, including that after the contact with water vapors [23]. The process of photoelectron emission is also shown schematically.

The level of attenuation of photoelectron emission for the K–Cs–Sb photocathode due to the covering CsBr nanofilm optimized from the point of view of protective properties can be judged by looking at Fig. 16 [26]: the quantum efficiency is reduced 5–10 times for the 280 Å thick film and is only 5% at the sensitivity maximum. This quantum efficiency is already of practical value.

3.2. Photoelectron Transport through Dielectric Nanofilms

For investigation of the transport characteristics of the nanofilm, it is deposited on the photocathode in several stages and the quantum efficiency is measured after each stage. The obtained dependence of the quantum efficiency on the nanofilm thickness is shown in Figs. 19 and 20 for opaque CsI and alkali–antimony photocathodes, respectively. For the CsI photocathode, the following types of dielectric films were studied: oxides SiO_2 and Al_2O_3 [23], fluorides CsF, NaF, LiF, and MgF_2 [23], iodide NaI [23], bromide CsBr [98], organic films hexatriacontane (HTC, n-$C_{36}H_{74}$) [23], and calcium stearate (CaSt) [99]. For alkali–antimony photocathodes, the following types of dielectric films were studied: for Cs–Sb photocathodes, CsI, NaI, CsF, SiO, HTC, and CaSt [25], for K–Cs–Sb photocathodes, CsBr [26, 28] and CsI [27, 98].

It can be seen that in some cases, the application of a film with a thickness of several atomic layers (5–10 Å) on the photocathode results in the sharp drop in the efficiency. For alkali–antimony photocathodes, this effect is observed for almost all types of films, while for the CsI photocathode, only for Al_2O_3. This effect is obviously due to the increase in the potential barrier at the photocathode/film and the film/vacuum interfaces.

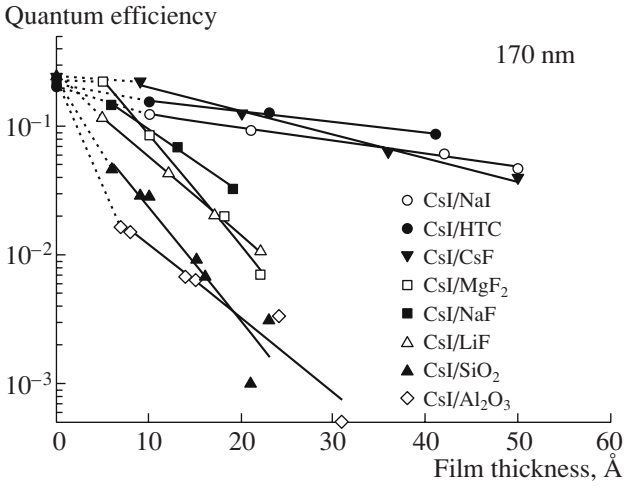

Fig. 19. Quantum efficiency for opaque CsI photocathodes in vacuum as a function of the thickness of nanofilms deposited on them at a wavelength of 170 nm. Data for NaI, HTC, CsF, MgF_2, NaF, LiF, SiO_2, and Al_2O_3 films [23] are shown.

At the same time, for film thicknesses larger than 5–10 Å, the quantum efficiency drops exponentially for all types of films; i.e., it is determined by the transport characteristics of the film. This provides the possibility of introducing the quantum efficiency attenuation length L in the film,

$$Y \sim \exp(-x/L),$$

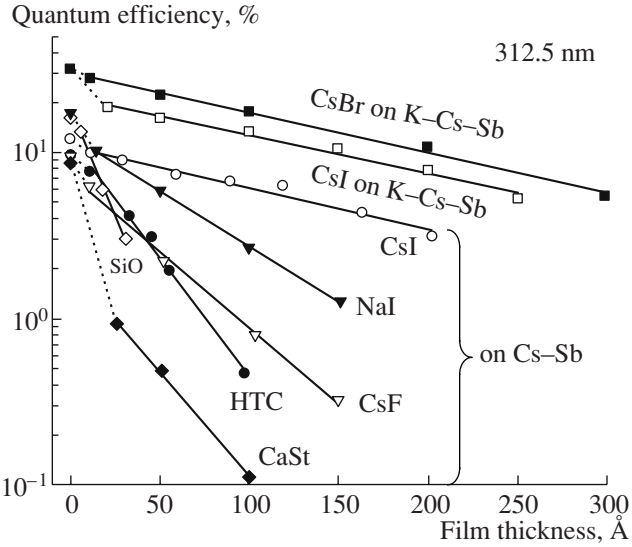

Fig. 20. Quantum efficiency for opaque alkali–antimony photocathodes in vacuum as a function of the thickness of nanofilms deposited on them at a wavelength of 312.5 nm. Data for CsI, NaI, CsF, SiO, HTC, and CaSt films on CsSb photocathodes [25] and CsBr [26] and CsI [27] films on K–Cs–Sb photocathodes are shown. Data of cited papers were refined and reprocessed.

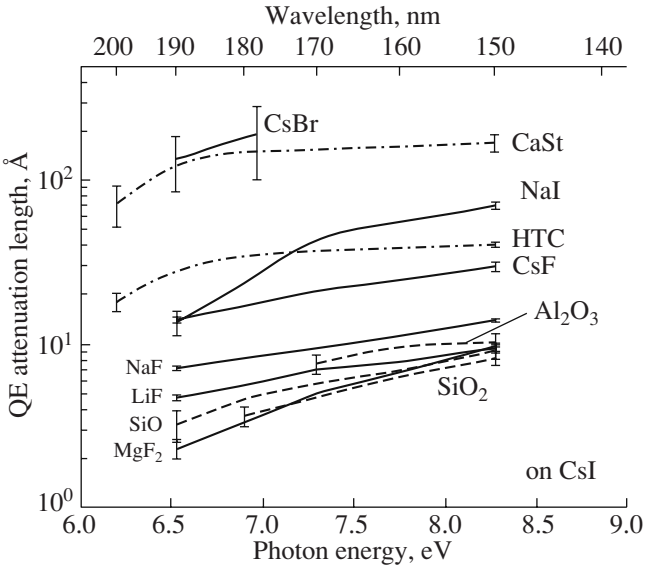

Fig. 21. Quantum efficiency attenuation length in different nanofilms deposited on opaque CsI photocathode as a function of the photon (lower scale) energy and (upper scale) wavelength [23]. Data for CaSt and CsBr films were taken from [25, 99] and [98], respectively. Data of cited papers were refined and reprocessed.

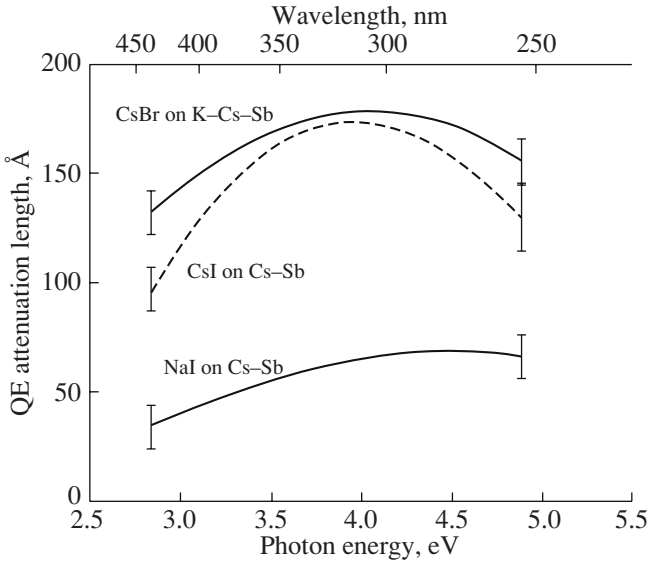

Fig. 22. Quantum efficiency attenuation length in CsBr, CsI, and NaI nanofilms deposited on opaque Cs–Sb and K–Cs–Sb photocathodes as a function of the photon (lower scale) energy and (upper scale) wavelength [25, 26]. Data of cited papers were refined and reprocessed.

where Y is the quantum efficiency of the photocathode coated with the film with the thickness x. The quantum efficiency attenuation length is related with the escape length L_{PE} and the photon absorption path L_{PH} in the film as

$$1/L = 1/L_{PE} + 1/L_{PH}.$$

If the film is transparent for photons, which is the case for almost all the studied materials, $L_{PE} = L_{PH}$.

Therefore, the quantum efficiency attenuation lengths in different nanofilms shown in Figs. 21 and 22 depending on the photon energy are actually the escape lengths. The data in Figs. 21 and 22 were obtained for CsI and alkali–antimony photocathodes, respectively. In both cases, the range of maximum photoelectron energy taking account of the width of the forbidden zone and the affinity to the electron is approximately the same and corresponds to 0.5–2 eV with respect to the vacuum level. This provides the possibility of investigation of the influence of the substrate on transport characteristics of the nanofilm in comparable energy ranges.

It can be seen from the analysis of the transport characteristics of nanofilms on CsI photocathodes (Figs. 19 and 21) that the difference in the escape length in different types of films can reach almost two orders of magnitude. In this case, three groups of films can be separated: films with large (100–200 Å), intermediate (20–70 Å), and small (up to 10 Å) escape length. The first group includes CsBr and CsSt, the second group, NaI, HTC, and CsF, and the third group, oxides and fluorides (with the exception of CsF).

It can be seen from the analysis of the characteristics of nanofilms on alkali–antimony photocathodes (Figs. 20 and 22) that high transport characteristics of CsBr and NaI are confirmed. The group of nanofilms with large photoelectron escape length is complemented with CsI. It is interesting that the order of magnitude of escape length is independent of the photocathode type; i.e., the transport properties in the first approximation are determined by the film material only. The sole exception is the CaSt film, whose transport characteristics deteriorate noticeably for Cs–Sb photocathodes as compared to CsI photocathodes.

It should be noted that the escape length in nanofilms measured using the alternative method with semitransparent ultraviolet photocathodes [100] and calculations performed using the microscopic model [98, 100] agrees satisfactorily with data in Figs. 21 and 22 (within a factor of 2).

The hypothesis on the dependence of the transport characteristics and protective properties of nanofilms on the matching of constants of crystal lattices of the photocathode and the film [26] should also be mentioned.

3.3. Influence of Nanofilms on Emission Properties of Photocathodes

There exist materials which, being applied as atomic layers on ultraviolet photocathodes, cause the enhancement of photoelectron emission. In this case, the photocathode activation, rather than the protective properties of nanofilms, is considered. Alkali metals [68] should obviously be included among these materials. It turned

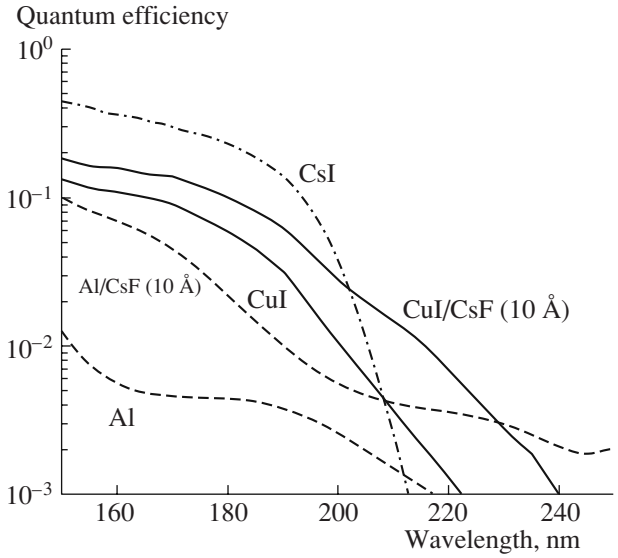

Fig. 23. Enhancement of the quantum efficiency for reflective photocathodes in vacuum using CsF nanofilm. Quantum efficiency spectra for CuI (after heat treatment) and Al photocathodes before and after the application of the CsF film with a thickness of 10 Å and the spectrum for the CsI photocathode [22] for comparison are shown.

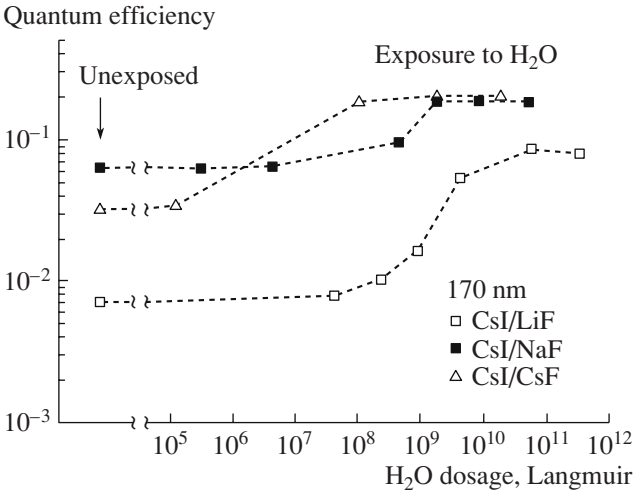

Fig. 24. Enhancement of the quantum efficiency for an opaque CsI photocathode coated with alkali–fluoride nanofilms obtained using water molecule adsorption. The quantum efficiency in vacuum for CsI/LiF (LiF thickness >15 Å), CsI/NaF (NaF thickness 15 Å), and CsI/CsF (CsF thickness 44 Å) at a wavelength of 170 nm is shown as a function of the exposure dose in water vapors (1 Langmuir = 10^{-6} Torr s) [23].

out that under certain conditions, CsF [22, 23] and water vapors [23, 102] can also be included. It is important to underline that, unlike alkali metals, the effect of quantum efficiency amplification for these materials was stable not only for the photocathode in vacuum but also in air [22, 23, 102].

It can be seen in Fig. 23 that the deposition of a 10 Å thick CsF film on the CuI photocathode results in a considerable increase in the quantum efficiency, especially in the long-wavelength region and the shift in the red boundary to 240 nm [22, 23]. As a result, at wavelengths larger than 210 nm the CuI photocathode becomes much more efficient than the CsI photocathode. For 220 nm, its efficiency is increased by one order of magnitude, which can be applied for readout of a BaF_2 scintillator whose maximum radiation for the fast component lies in this particular range [92].

It is interesting that the effect of quantum efficiency amplification due to the deposition of CsF is observed for the Al photocathode (Fig. 23) [22] and is practically not observed for the CsI photocathode [23]. The effect of the action of CsF is probably explained by the decreased work function of the photocathode due to partial dissociation of CsF on its surface [101].

It is interesting that the effect of photoelectron emission amplification can be observed during absorption of molecules of such common material as water, namely, at its adsorption at the surface of alkali–fluoride films. This effect was observed after exposure of the CsI photocathode coated with LiF, NaF, and CsF nanofilms in water vapors [23, 102]: after a certain exposure dose, the quantum efficiency was increased several times (Fig. 24). The enhancement of photoelectron emission is explained by the decreased work function of the film by approximately 0.4 eV (see Fig. 18) due to the polarization of dipoles of the water molecules at adsorption [23].

This effect has not been applied in practice yet, since the efficiency of the CsI photocathode coated with the alkali–fluoride nanofilm, even after activation using water vapors, practically does not exceed the efficiency of the uncovered CsI cathode. Nonetheless, it opens new possibilities in the search for efficient photocathodes that are stable in air, specifically, the search for materials with a large molecular dipole moment that can be polarized by adsorption on the photocathode.

Another interesting effect was discovered when photocathodes for the visible range were coated with the organic film hexatriacontane [29]. Hexatriacontane (HTC, n-$C_{36}H_{74}$) belongs to the class of paraffins. Its specific feature is a rather low temperature of sublimation in vacuum. For example, an HTC film with a thickness of 1 μm deposited on the photocathode can be removed from it by heating at a temperature of 130–150°C in only 15 min [29]. At the same time, the limit of the temperature stability for the Cs–Sb photocathode is 130–150°C [29], and that for bi-alkali photocathodes is even higher [68]. Another remarkable property of HTC is its chemical inertness with respect to alkali–antimony photocathodes: their emission characteristics are not changed after the contact with HTC. Both properties are illustrated in Fig. 25: after two cycles of deposition and removal of HTC films with a thickness of up

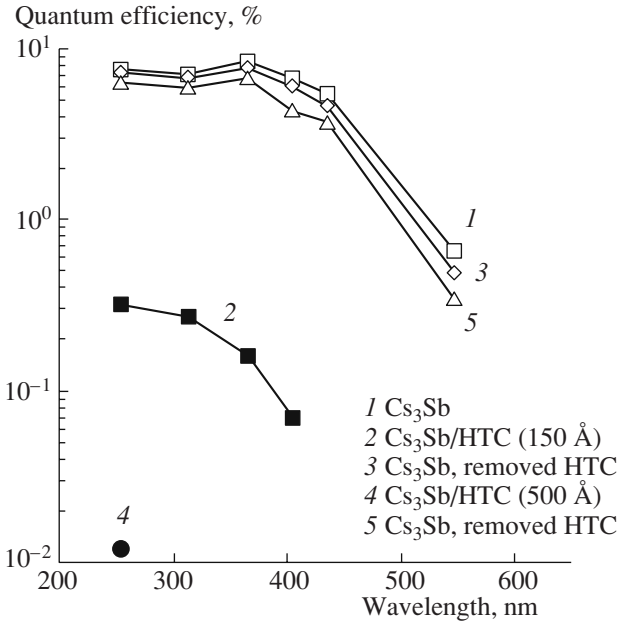

Fig. 25. Evolution of the quantum efficiency spectrum for opaque Cs–Sb photocathode in vacuum as a result of two cycles of deposition and removal by heating of HTC films (n-$C_{36}H_{74}$) with a thickness of 150 and 500 Å [29].

to 500 Å, the quantum efficiency of the Cs–Sb photocathode was practically unchanged [29].

The thickness of the HTC films optimal from the point of view of protection from oxygen turned out to be up to 1 μm; thicker films were peeled off the photocathode due to internal stresses [29]. This film thickness may be quite sufficient for complete protection of the photocathode from oxygen (and possibly from water vapors as well, due to the hydrophobic character of paraffins).

HTC films can be used as a removable (i.e., temporary) protective coating for photocathodes for the visible range. Obviously, the sublimation temperature of the removed protective film can be reduced, and, therefore, the effect of this procedure on the photocathode can be mitigated if lighter paraffins are used.

Removable organic coatings could provide a possibility of transportation of photocathodes for the visible range through air or poor vacuum, which could considerably simplify the procedure of assembling both vacuum and gaseous photodetectors. Removable coatings on CsI photocathodes could considerably extend their storage time, including that in air.

3.4. Protective Properties of Nanofilms on Photocathodes for the Visible Range

High sensitivity of photocathodes in the visible range in general, and alkali–antimony photocathodes in particular, to admixtures of oxygen and water vapors seriously complicates their use in GPD. The sensitivity

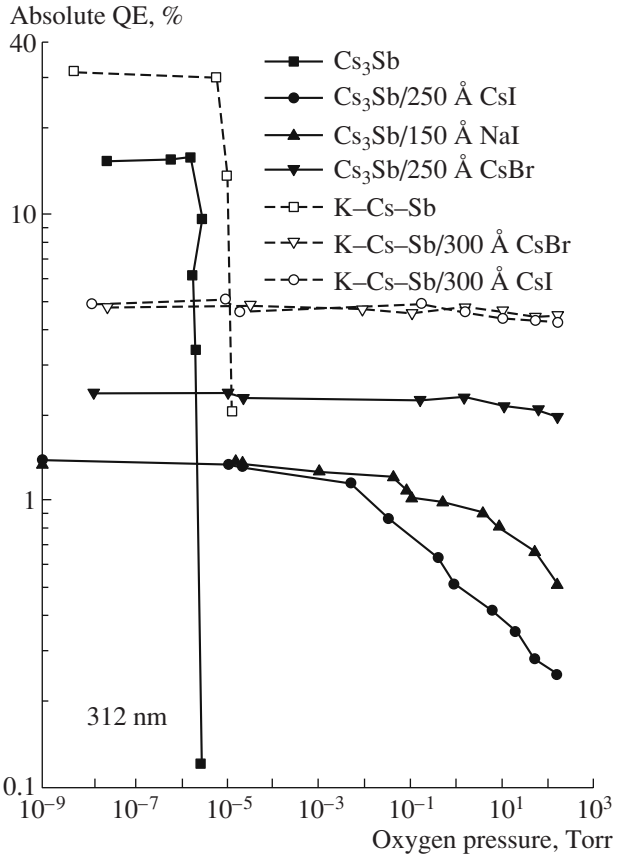

Fig. 26. Protective properties with respect to oxygen of nanofilms on reflective photocathodes for the visible range. The evolution of the quantum efficiency of unprotected Cs–Sb and K–Cs–Sb photocathodes and photocathodes protected by CsBr, CsI, and NaI films at a wavelength of 312 nm is shown as a function of oxygen pressure [27]. Each point corresponds to the photocathode exposure in oxygen for 5 min and subsequent measurement of the quantum efficiency in vacuum.

of Cs–Sb and K–Cs–Sb photocathodes is illustrated in Fig. 26: photocathodes completely lose efficiency even at 10^{-5} Torr of oxygen [27]. Therefore, investigation of the protective properties of nanofilms on photocathodes in the visible range is of primary importance.

It turned out that only three types of nanofilms provide efficient protection of alkali–antimony photocathodes from oxygen; these are CsBr [26], CsI [25, 27], and NaI [24, 25]. The same films, as shown in Section 3.3, have the best characteristics for photoelectron transport. The protective capability of other studied nanofilms (oxides, fluorides, and organic nanofilms) turned out to be unsatisfactory [25].

The procedure of investigation of the protective capability of nanofilms consisted of several consecutive cycles of measurement. Each cycle included the exposure of the photocathode with the protective film in oxygen for 5 min at a particular pressure and subsequent measurement of its quantum efficiency in vacuum. The obtained dependence of the quantum effi-

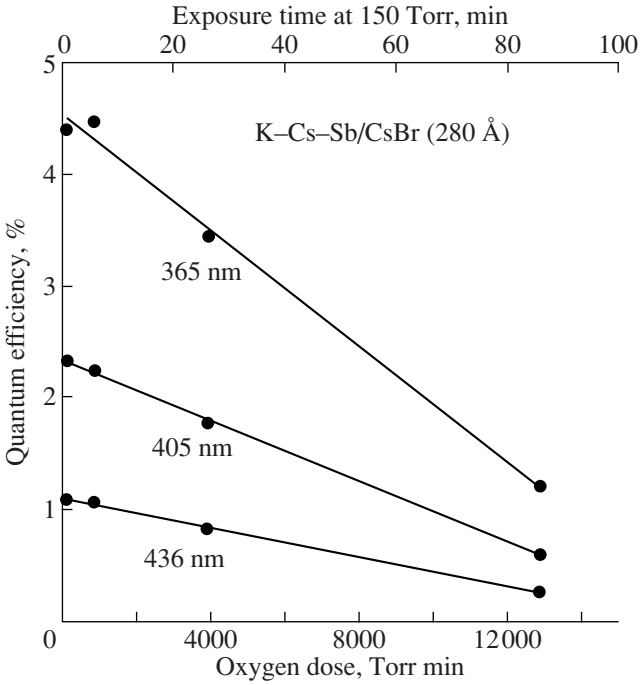

Fig. 27. Protective properties with respect to oxygen of CsBr nanofilm on opaque K–Cs–Sb photocathode. The evolution of the quantum efficiency for K–Cs–Sb photocathode coated with CsBr film with a thickness of 280 Å at different wavelengths is shown as a function of exposure time in oxygen at pressure of 150 Torr (upper scale) [26]. Data of cited works were reprocessed.

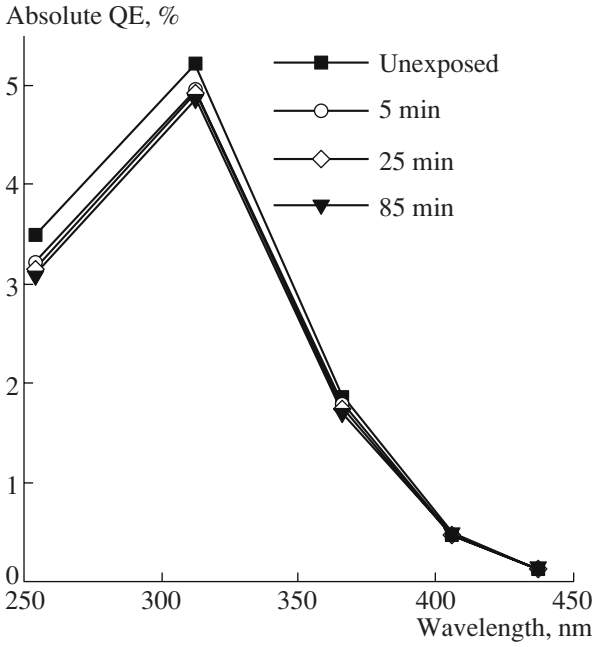

Fig. 28. Protective properties with respect to oxygen of CsI nanofilm on opaque K–Cs–Sb photocathode. The evolution of quantum efficiency spectra for K–Cs–Sb photocathode coated with CsI film with a thickness of 250 Å after exposure in oxygen at pressure of 150 Torr for 0, 5, 25, and 85 min [27] is shown.

ciency on oxygen pressure is shown in Fig. 26 [27]. The last points in this figure correspond to exposure at a pressure equal to the partial pressure of oxygen in air (150 Torr).

It turned out that for efficient protection of photocathodes by nanofilms, thicknesses larger than 150 Å for NaI [25] and larger than 250 Å for CsI [25, 27] and CsBr [26] are required. For these thicknesses, the quantum efficiency of protected photocathodes is still sufficiently high and corresponds to about 5–7% for K–Cs–Sb and 2–3% for Cs–Sb in the range 300–350 nm. It can be seen from Fig. 26 that the best protective capability for both types of alkali–antimony photocathodes is possessed by CsBr nanofilms, and for the K–Cs–SB photocathode by the CsI film.

The remarkably efficient protection of K–Cs–Sb photocathodes from oxygen using nanofilms can be judged from Figs. 27 and 28, and for Cs–Sb photocathodes from Fig. 29. Figure 27 shows the dependence of the quantum efficiency of the K–Cs–Sb photocathode coated with the CsBr nanofilm on the time of exposure in oxygen at pressure of 150 Torr [26]; even after one and a half hours of exposure, the quantum efficiency was still higher than 1%. Even more stable behavior was observed for the K–Cs–Sb photocathode coated with the CsI nanofilm [27]: during one and a half hours in oxygen, the spectrum of the quantum efficiency was practically unchanged (Fig. 28). It can be concluded from the comparison of Figs. 27–29 that the most efficient and protected from the action of oxygen are the K–Cs–Sb photocathodes coated with CsBr or CsI nanofilms.

The mechanism of photocathode protection from oxygen using CsBr and NaI nanofilms is not yet clear. It is possible that its action is due to the oxidation of alkali–halide films and formation of a stable protective oxide layer of the type $CsBrO_3$, $CsIO_3$, or $NaIO_3$ [26]. It is well known that the natural oxide layers with a thickness of only 20–40 Å formed on the surface of aluminum and silicon are capable of protecting them from further oxidation.

The penetration of oxygen through the nanofilm has diffuse character. This is proved by the linear dependence of the decrease in the quantum efficiency from the dose of exposure (see Fig. 27). This behavior is similar to the gas diffusion through membranes (see, e.g., [103]). It is described by the corresponding model; in particular, such a notion as the permeability of the film for a particular type of molecules can be introduced.

Unlike efficient protection from oxygen, alkali–halide nanofilms were incapable of ensuring sufficiently efficient protection from water vapors. For example, K–Cs–Sb photocathodes coated with CsBr or CsI nanofilms degraded completely at a water vapor pressure of 10^{-4}–10^{-4} Torr [28]. This result, obviously, is explained by the hydrophilic character of the alkali–halide compounds. The Cs–Sb photocathode coated with the NaI nanofilm demonstrated higher stability [24];

although the quantum efficiency decreased considerably after the exposure in air at a water vapor pressure of 10^{-2} Torr, it was completely restored after the photocathode was heated (Fig. 29).

There exists another application of CsBr and CsI nanofilms: attenuation of the ion feedback in GPD with photocathodes for the visible range. It is considered in Section 4.3.

In conclusion to this section, it should be noted that the efficient protection of alkali–antimony photocathodes from oxygen and to a smaller degree from water vapors using nanofilms provides the possibility of considerable simplification, and in some cases fundamental improvement, of different procedures with photocathodes upon photodetector assembly. In particular, manipulations with these photocathodes may be performed in industrial dry glove boxes in which water vapor content can be easily made smaller than 10^{-6}.

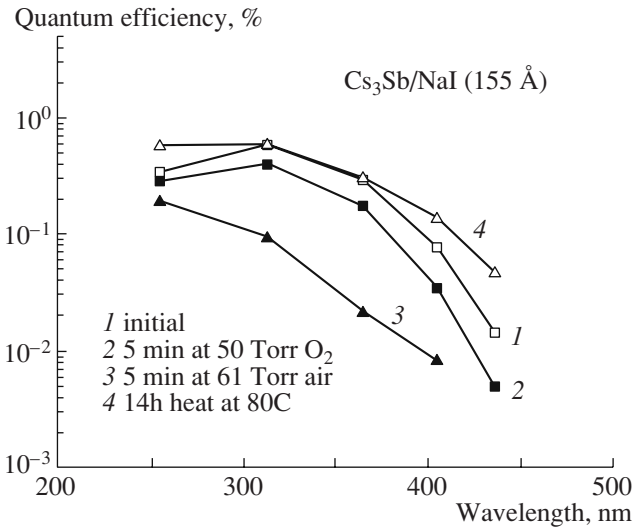

Fig. 29. Protective properties with respect to oxygen and water vapors of NaI nanofilm on opaque Cs–Sb photocathode. The evolution of quantum efficiency spectra for Cs–Sb photocathode coated with NaI film with a thickness of 155 Å is shown: (*1*) initial spectrum; (*2*) after exposure in oxygen at pressure of 50 Torr during 5 min; (*3*) after exposure in air at pressure of 61 Torr with a partial pressure of water vapors of 10^{-2} Torr for 5 min; (*4*) after heating in vacuum at 80°C for 14 h [24].

4. GAS ELECTRON MULTIPLIER BASED GPDS

4.1. The Physics of Multistage GEM in GPD

The advantages of multistage GEMs and the principles of operation of GPDs based on them were discussed in Section 1. In this section, the characteristics of different types of GEM-based GPDs are considered in detail.

The operation and application of GEMs are based on different physical effects [34]. An especially large number of these effects are observed in detectors containing multistage GEMs and a photocathode which operate in pure noble gases [11, 104]. Figure 3 shows schematically some of these effects, as exemplified by the GPD with the semitransparent photocathode [58]:

(i) photoelectron backscattering to the photocathode, which results in a decrease in the photocathode quantum efficiency in gas as compared to vacuum [11, 12, 46–48] (see Section 2.3);

(ii) photon feedback to the photocathode due to the avalanche scintillation in GEM holes and proportional scintillations in the drift gap, which results in secondary pulses [11, 12];

(iii) ion feedback of GEM to previous GEMs and the photocathode, which causes ion-induced electron emission resulting in secondary pulses and thus limits maximum gain [11, 58, 104];

(iv) ion backflow to previous GEMs and the photocathode, which results in charging-up of the dielectric surface of GEM holes and the photocathode surface at large anode current densities and, thus, amplification instability [11, 104, 105];

(v) confinement of the spatial development of the avalanche inside the GEM hole, resulting in the absence of optical coupling between the holes and avalanche saturation at relatively moderate gains [11, 104], which provides GEM operation in pure noble gases with high gain;

(vi) avalanche extension from the hole or inside it at high gains [11, 104], which results in a decrease in ion feedback [64] and limitation to the minimum distance between GEMs.

Other effects related to the operation of multistage GEMs in GPDs were also studied: the breakdown mechanisms in multistage GEMs [106, 107], the efficiency of photoelectron collection in GEMs in GPDs with semitransparent [108] and opaque [13] photocathodes, the electron [63] and ion [16, 63–65, 109] transmission by multistage GEMs, the photocathode aging in GEM-based GPDs for the ultraviolet [16, 69] and the visible [21, 28] ranges, the measurement of the ionization coefficients in dense noble gases using GEMs [34], and so on. It can be said that GEM-based GPDs are beyond competition among gaseous detectors, as regards the variety of physical phenomena in them. This allows them to serve as a tutorial for investigation of the physics of gaseous detectors.

4.2. GEM-Based GPDs with CsI Photocathodes

One of the most important stages of development of GPDs with the CsI photocathode was the investigation of its characteristics for optimization of different parameters, such as the gas composition, the photocathode type, and the configuration of GEM cascades. At this stage, fundamental properties of GPDs characteristic for gaseous photodetectors in general were studied. These investigations were performed by using relatively simple and multipurpose setups for which it was possible to change the parameters of measurements

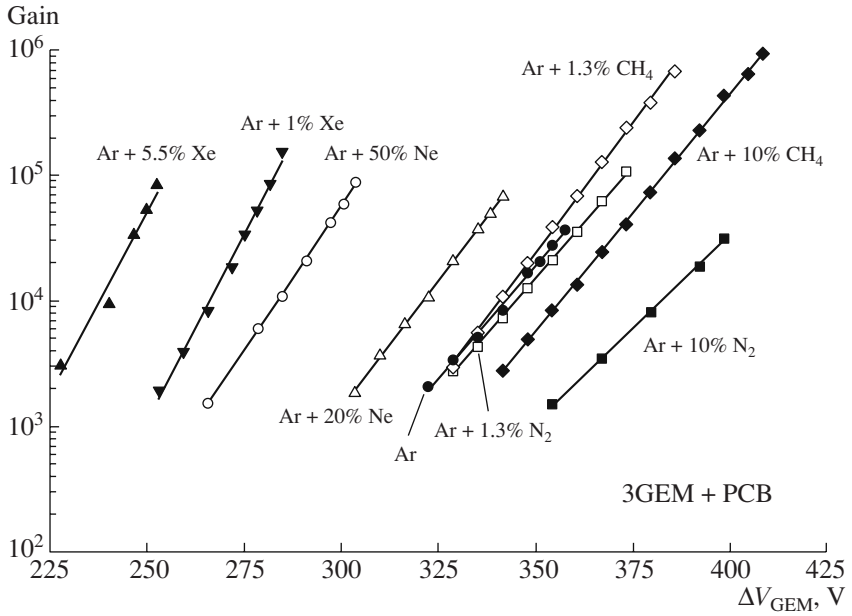

Fig. 30. Gain for three-stage GEM-based GPD with semitransparent CsI photocathode as a function of voltage on each GEM in different Ar-based gas mixtures at atmospheric pressure [11]. Maximum gain is limited by breakdown.

promptly. This setup usually represented the pumped chamber, including the flanges with the quartz window and the connectors inside which the GPD itself was placed [11].

The GEM-based GPD was first studied in 2000 at such a setup [11]; the semitransparent CsI photocathode and 3–4 GEM cascades were used in it. The schematic diagram of this GPD is shown in Fig. 2. Such GPD characteristics as the amplification, the single-electron spectra, the photoelectron backscattering to the photocathode, the photon and ion feedback, the charging-up by the ion backflow, and the photocathode aging were studied [11, 12, 15, 16, 104]. Some of these characteristics are considered below.

The unique property of multistage GEMs is their capability of operating with high gain in pure noble gases. This capability is of special interest for development of sealed GPDs with chemically active photocathodes for the visible range [15, 20], since in this case, no active radicals which can damage the photocathode are formed in the avalanche. The operation in pure noble gases is also necessary in different cryogenic avalanche detectors [38, 39, 59–62, 110–112], in which the application of the molecular quenching admixture is impossible due to low temperature.

Figure 30 shows the amplification characteristics of the GPD based on the three-stage GEM and the semitransparent CsI photocathode in pure Ar and its mixtures with other noble gases and some molecular gases [11]. Hereinafter, data are presented at atmospheric pressure unless indicated otherwise. It can be seen that multistage GEMs can possess rather high gain, on the order of tens of thousands in pure Ar and 10^5 in mixtures of it with Xe, Ne, and N_2. This exceeds the maximum gain achieved in pure Ar for other gaseous detectors, in particular proportional counters [113], by two or more orders of magnitude. It can also be seen that in mixtures of Ar with quenching admixtures, a gain on the order of 10^6 is easily achieved.

It should be noted that data in Fig. 30 take into account only the fast primary component of the anode signal due to avalanche amplification. If the slow secondary component of the signal due to photon feedback resulting from proportional scintillations in the drift gap and the avalanche radiation in the GEM holes is also taken into account, the gain in Ar and its mixtures with Xe and Ne is increased several times, reaching 10^6 [11].

It turned out that GEMs can operate with high gain not only in Ar but in other noble gases as well [34], and also in high pressure conditions [58, 114–116]. Especially high gain was obtained in the Penning mixtures He + Kr [116], He + N_2 [117], He + H_2 [112], and Ne + H_2 [60]: the gain of the three-stage GEM in some of these mixtures could exceed 10^6.

High gain achieved in GPDs based on multistage GEMs provides efficient operation in the single photon counting mode. Figure 31 shows the amplitude spectra obtained in this mode using the charge amplifier at gas gains of $(2–4) \times 10^5$ [11]. The shape of the spectrum of the single-electron signal provides the possibility of judging on the mechanism of the avalanche development. The exponential shape observed in Ar is most typical for gaseous detectors at moderate gains; it testifies that the ionization acts in the avalanche are independent [118]. The deviation from the exponential shape of the spectrum due to the increased contribution

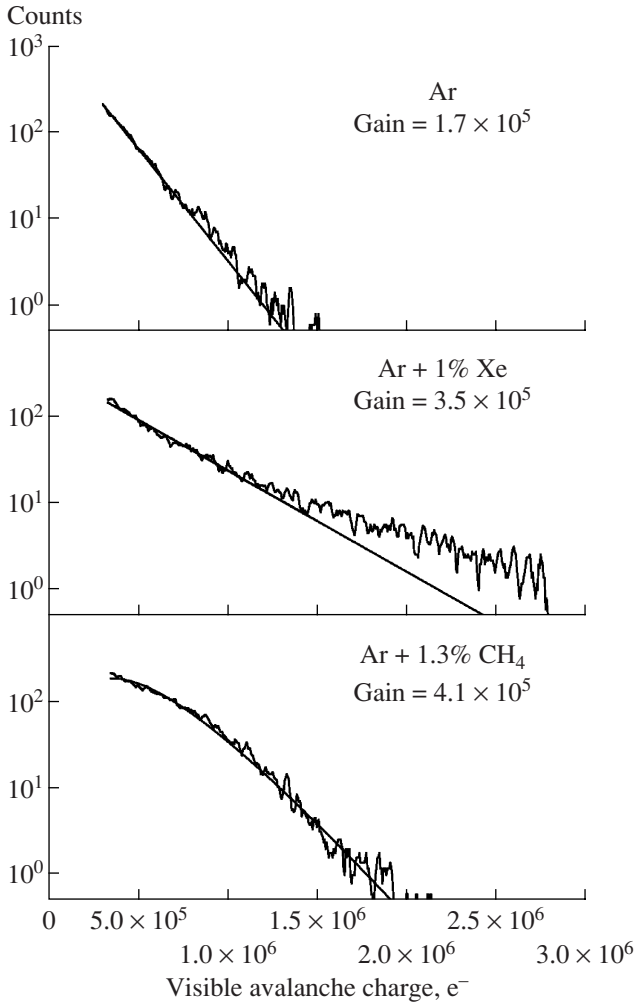

Fig. 31. Amplitude spectra of anode signals from three-stage GEM-based GPD with semitransparent CsI photocathode in the single photoelectron counting mode in Ar, Ar + 1% Xe, and Ar + 1.3% CH_4 for a gain of $(2–4) \times 10^5$ [11].

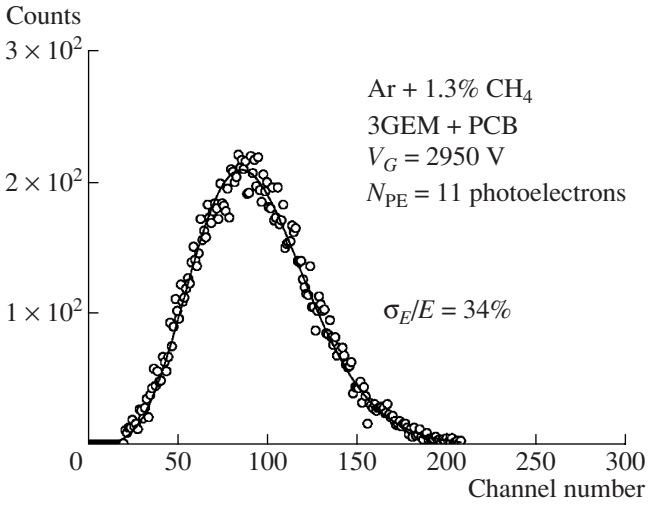

Fig. 32. Amplitude spectrum of anode signals from three-stage GEM-based GPD with semitransparent CsI photocathode for 11 photoelectrons in Ar + 1.3% CH_4 for a gain of 2×10^5 [11].

of large amplitudes testifies to the considerable role of secondary processes in the avalanche; this shape is observed, for example, in Ar + Xe. The opposite deviation from the exponential shape observed in Ar + CH_4 is described by the Polya distribution and testifies the avalanche saturation when ionization acts become correlated [118]. This effect occurs probably as a result of increasing avalanche density due to the limitation of its spatial development in the GEM hole [11], i.e., the avalanche "confinement" [88].

Since the single-photoelectron spectrum in GPD has mainly exponential shape, the amplitude resolution in GPD is worse than in PMT for small photoelectron statistics. Nonetheless, for a number of photons on the order of 10, the amplitude resolution is rather high and makes about 30%, which is close to the statistical limit (see also Fig. 32).

The highest gain, almost 10^7 [12], was obtained in GEM-based GPDs in CF_4. This is seen in Fig. 33, which shows the gain characteristic in CF_4 in comparison with other gases. Such a high gain provided efficient operation in the single photon counting mode using fast current amplifiers (and not only charge amplifiers), which is important for time measurements. The operation of GEM-based GPDs in CF_4 has other advantages, as compared to other gases: the signal in it is the fastest (the FWHM is 8 ns), and the photoelectron backscattering to the photocathode is minimum (see Section 2.3). It should be pointed out that the voltage necessary for operation in pure CF_4 is rather high, exceeding the working voltage in other gas mixtures by a factor of approximately 1.5. This probably means that thicker amplification structures with holes, such as thick GEMs [56, 57] and capillary plates [53, 54], would be unlikely to operate successfully in pure CF_4 due to breakdowns.

High time resolution of GEM-based GPDs in CF_4 is illustrated in Fig. 34; this figure shows the time spectra for different number of photoelectrons. The time resolution is 2 ns in the single photoelectron mode and 0.33 ns for 150 photoelectrons, which is probably the record for gaseous detectors operating in the proportional mode. As was already noted in Section 1, it is these remarkable characteristics that served as the basis for development of the Cherenkov counter operating in pure CF_4 for the experiment PHENIX [35–37].

The characteristics of the GPD with semitransparent CsI photocathode were considered above. The characteristics of GEM-based GPD with opaque CsI photocathode deposited on the electrode of the first GEM (see Fig. 4) were studied in detail in [13]. Figure 35 illustrates the most characteristic property of GPDs of this type, namely, the efficiency of photoelectron collection from the photocathode and the GEM hole,

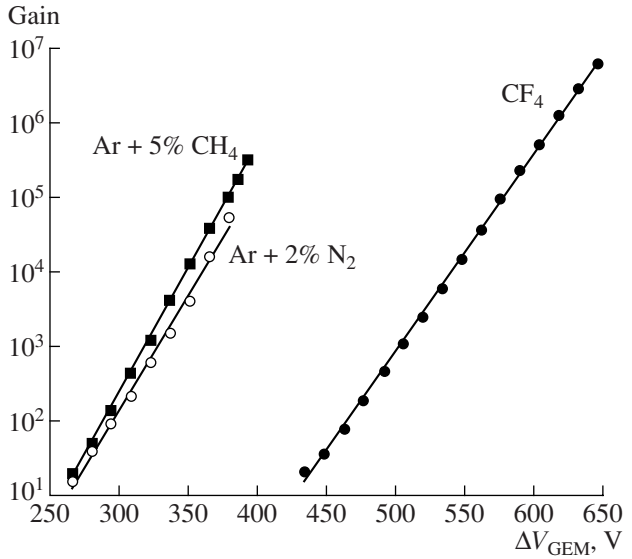

Fig. 33. Gain of three-stage GEM-based GPD with semitransparent CsI photocathode as a function of voltage on each GEM in CF_4, Ar + 5% CH_4, and Ar + 2% N_2 at atmospheric pressure [12]. Maximum gain is limited by breakdown.

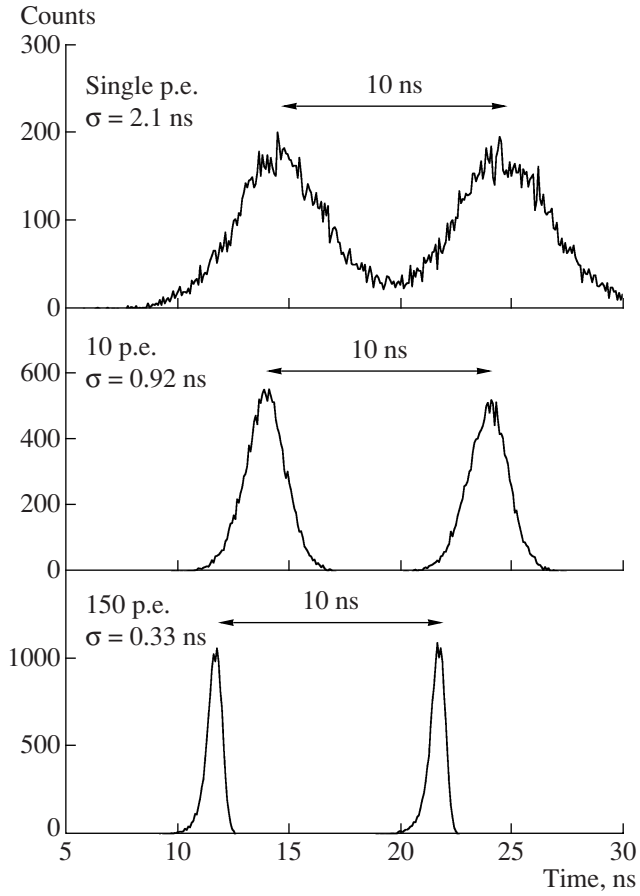

Fig. 34. Time characteristics of anode signals from three-stage GEM-based GPD with semitransparent CsI photocathode with CF_4 in the single photoelectron counting mode and also for 10 and 150 photoelectrons and a gain of 10^6 [12]. Time distributions with respect to the trigger of two groups of pulses separated by a 10 ns interval are shown.

which is described by the dependence of the anode current from the drift field. As expected from the pattern of the force lines shown in Fig. 4 [14], photoelectrons are most efficiently focused in GEM holes at zero drift field [13].

The coordinate characteristics of GEM-based GPDs with CsI photocathodes were studied in [14, 119]. In [14], a spatial resolution of 55 μm for single photons upon readout to the anode in the form of parallel strips was obtained. In [119], the record degree of localization of single photons with a precision of 4 μm upon readout to the anode in the form of pixels, where each pixel represented a miniature integrated circuit, was obtained. Variants of coordinate readout of GPDs using the delay line [120] and the zigzag-shaped anode [121] were also considered.

The principles of operation of GEM-based GPDs with reflective photocathodes and the capability of multistage GEMs to operate with high gain in pure noble gases were used in the cryogenic two-phase avalanche detectors considered in Section 1. The schematic diagram of these detectors is shown in Fig. 5. Figure 36 shows the amplitude spectra of the three-stage GEM in two-phase Ar obtained with this schematic diagram in the single photoelectron counting mode [62]. For gains of 6×10^3 and 1.7×10^4, the spectrum is separated well from the electronics noise. This provides the possibility of speaking of efficient GPD operation in the single-photoelectron mode in two-phase Ar beginning from gains of order of 5×10^3.

The operation of GEM-based GPDs with opaque CsI photocathodes in two-phase Ar in the mode of simultaneous detection of scintillation and ionization signals was recently demonstrated [39]. This detection method would allow identification of events due to the recoil of nuclei in collisions with dark matter [41, 42] or coherently scattered neutrinos [40]. In the case of PET, it would provide the possibility of organization of a fast trigger for coincidences between two photons [43, 44]. Figure 37 shows the two-dimensional event distribution with respect to the amplitudes of the scintillation and the ionization signals upon irradiation by β particles with a particular energy in a liquid of about 600 keV [39]. Clear correlation, namely, proportionality between the scintillation and the ionization signals, is observed. In this case, the amplitude of the scintillation signal was 30 photoelectrons, which is quite sufficient for PET but is too little for the search of dark matter. The investigations in this direction continue.

An important stage in development of GEM-based GPDs was the development of sealed devices. The first sealed GEM-based GPD was produced in 2001 (Figs. 38, 39) [15, 16]. In this device, the semitransparent CsI photocathode and the cascade of four GEMs

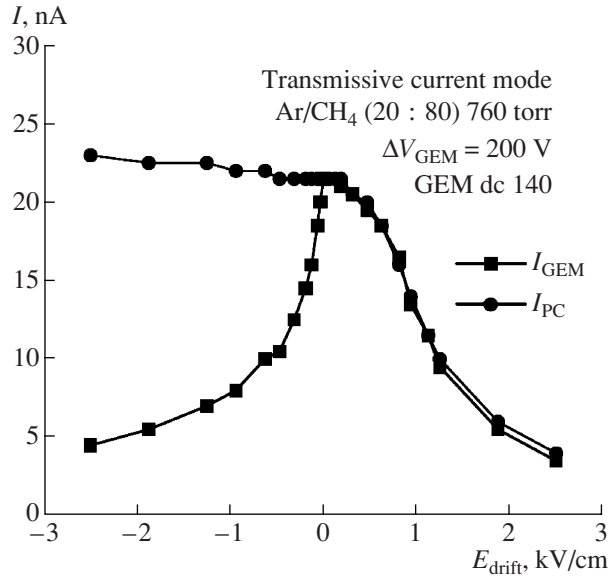

Fig. 35. The influence of the drift field on efficiency of photoelectron collection in GEM hole from the opaque CsI photocathode deposited on GEM [13]. The anode and cathode GEM currents are shown as functions of drift field strength in Ar + 80% CH_4 for a voltage at GEM of 200 V.

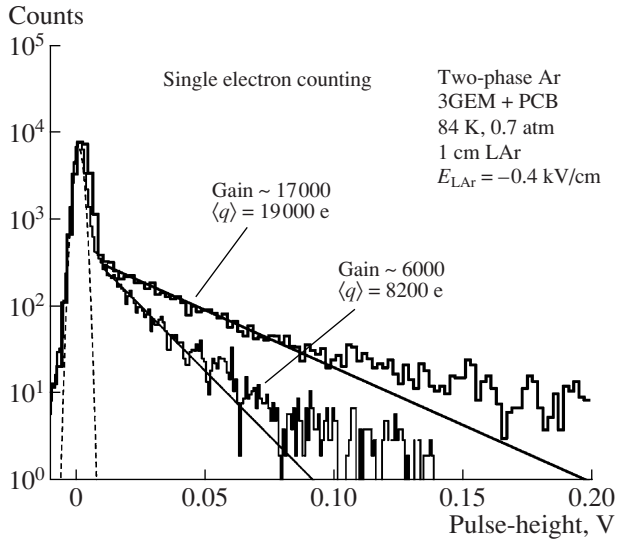

Fig. 36. (Solid lines) Amplitude spectra of the anode signal from three-stage GEM in two-phase Ar in the single photoelectron counting mode at 84 K, 0.7 atm, and gains of 6×10^3 and 1.7×10^4, and (dashed lines) spectrum of noises from the readout electronics [62]. The first electrode of the first GEM was used as the reflective photocathode (see Fig. 5).

was used. The detector was produced using the method of photocathode transfer through vacuum using a specialized setup [20]. The principle of operation of this setup is similar to that of the setup shown in Fig. 15; however, its design was much more complicated: the procedures of the photocathode preparation, quantum efficiency measurement, and photodetector sealing were performed in different vacuum chambers, and the photocathode was transferred between these chambers using the manipulator.

The sealed GPD consisted of the package made from Kovar with several insulated contacts for voltage supply and signal readout. Inside the package, the multistage GEM was mounted on ceramic frames (Fig. 38). The important stage of production of the sealed GPD was the sealing procedure [15, 20], during which the quartz window was soldered to the package using an indium-based solder at a temperature of 120–150°C (Fig. 39). GPD operated with the Ar + 5% CH_4 mixture and had a gain of larger than 10^5 [15].

The main result of this stage was the fact of compatibility of GEM with the technology of sealed devices. It was shown that GEM withstands heating in vacuum at 200°C, and the photocathode of the sealed GPD is not damaged in the presence of GEM.

4.3. Sealed GEM-Based GDPs with a Photocathode for the Visible Range

Obviously, photocathodes for the visible range can be stable only in sealed GPDs. The method of production of sealed gaseous photodetectors tested using GPDs with the CsI photocathode was successfully used for production of sealed GPDs with photocathodes for the visible range [18–21].

The characteristics of the sealed GPD based on multistage GEM with the semitransparent K–Cs–Sb photo-

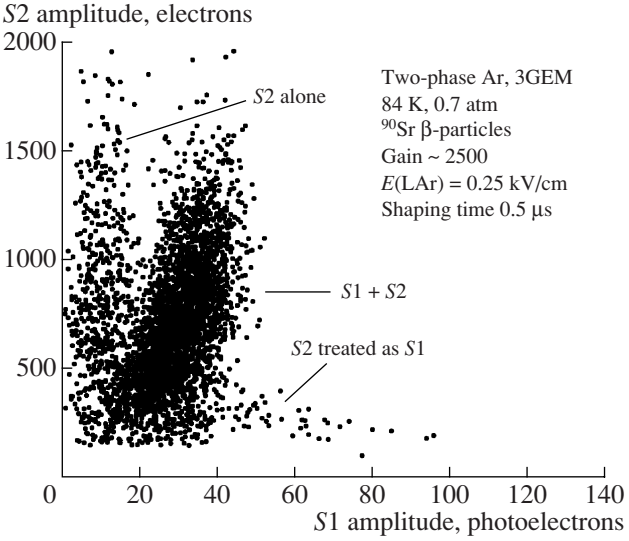

Fig. 37. Two-dimensional amplitude distribution for the (S1) scintillation and (S2) ionization signals from three-stage GEM-based GPD with opaque CsI photocathode in two-phase Ar at 84 K, 0.7 atm, and a gain of 2.5×10^3, for irradiation by β particles with an average energy in the liquid of 600 keV [39]. Amplitudes are expressed in numbers of photoelectrons and electrons, respectively. The first electrode of the first GEM coated with CsI was used as the reflective photocathode (see Fig. 5).

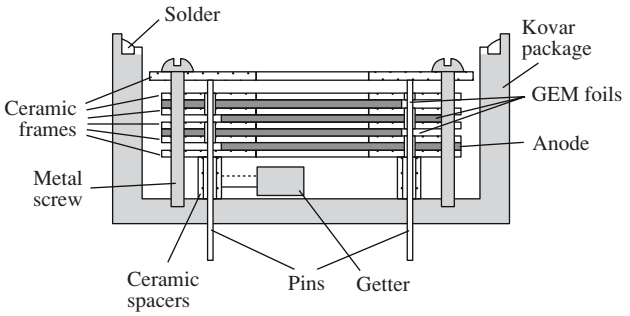

Fig. 38. Schematic diagram of the internal part of sealed three-stage GEM-based GPD [20].

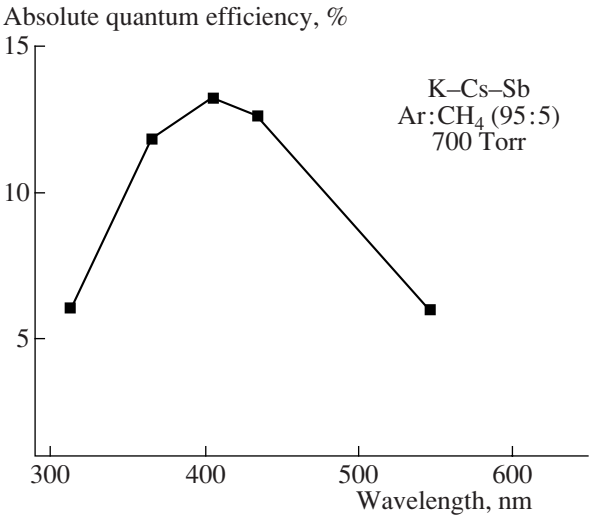

Fig. 40. Quantum efficiency spectrum for semitransparent K–Cs–Sb photocathode in sealed multistage GEM-based GPD in Ar + 5% CH_4 at pressure of 700 Torr [18, 20]. The drift field at the photocathode is 0.5 kV/cm.

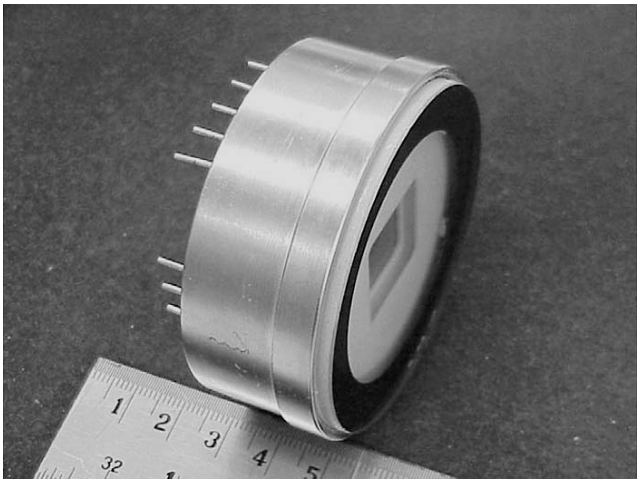

Fig. 39. View of the sealed four-stage GEM-based GPD with semitransparent CsI photocathode [15, 16].

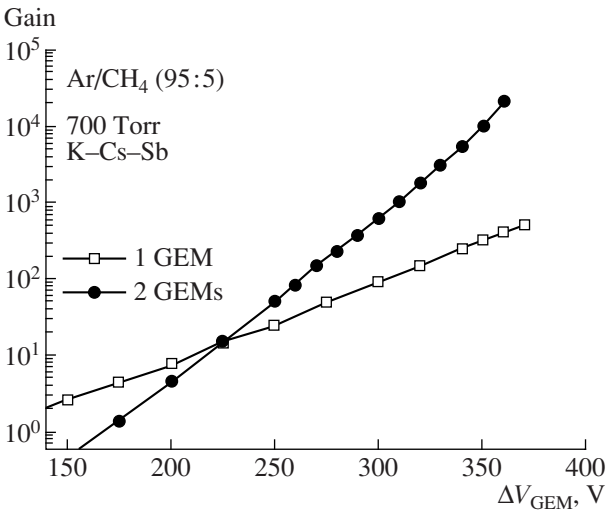

Fig. 41. Gain for sealed multistage GEM-based GPD with semitransparent K–Cs–Sb photocathode as a function of voltage on each GEM in Ar + 5% CH_4 at a pressure of 700 Torr in the configuration with the single-stage (1 GEM) and two-cascade (2 GEM) GEM [18, 20].

cathode operating with the Ar + 5% CH_4 mixture are illustrated in Figs. 40 and 41 [18, 20]: impressive results for the quantum efficiency, up to 13% at the maximum (Fig. 40), and gain, up to 10^4 for the two-stage GEM (Fig. 41), were obtained. It was demonstrated in the mode without amplification that the photocathode quantum efficiency is stable for several months if the getter inside the device is used [20]. In the amplification mode, the duration of operation turned out to be on the same order as that for GPD with the CsI photocathode (see Section 4.4): the quantum efficiency of the GPD with the K–Cs–Sb photocathode was decreased by 20% after a charge of 2 μC/mm^2 had passed at the anode, which corresponds to 10 years of operation for a gain of 10^5 and a photon current of 1 kHz/mm^2 [21].

For further development of sealed GPDs with photocathodes for the visible range, there are several problems of both technical and physical character. In particular, the sealing procedure has not been developed yet, and as a result, in most cases, the K–Cs–Sb photocathode lost efficiency due to high temperature necessary for the sealed coupling of the package and the window [20]. This problem can be solved by the transition to the sealing technology at room temperature used by a number of companies for production of vacuum photodetectors using the method of photocathode transfer.

Another problem was the increased sensitivity of photocathodes for the visible range to the ion feedback [20, 21]. Due to the increased sensitivity, the GPD gain in Ar, CH_4, and their mixtures in most cases did not exceed several hundred for the K–Cs–Sb photocathode [20]. The effect of the ion feedback is manifested in the occurrence of the secondary pulses and the deviation from the exponential dependence of gain on voltage at

high values (see Section 4.4). At the same time, the effect of the ion feedback in some cases was unnoticeable even for gains on the order of 10^4 in GEM-based GPDs [18, 20] (see Fig. 41) and in GPDs based on capillary plates [122]. Obviously, the problem of how the maximum GPD gain is limited by the ion feedback requires further investigation.

It should be noted that for the CsI photocathode, the ion feedback began to be manifested only for a gain of larger than 10^5 [11]. The difference between CsI and K–Cs–Sb is probably due to large coefficient of ion-induced electron emission (which is the reason for the ion feedback [123]) for photocathodes for the visible range due to lower threshold of photoelectron emission.

In this regard, the possible solution of the problem of the ion feedback is the coating of the photocathodes for the visible range by CsBr and CsI nanofilms. These films, along with the effect of the photocathode protection from active molecules considered in Section 3, can also attenuate the ion feedback. Indeed, the ion-induced electron emission will then be determined by the material of the nanofilm, rather than that of the photocathode. This conclusion is proved by the data shown in Fig. 42: in GPD with the K–Cs–Sb photocathode coated with the CsBr nanofilm, the ion feedback in pure CH_4 was not observed even for a gain of 2×10^4 [28]. It should be noted that if it is not required to transfer the photocathode through air, the protective film can be made thinner, for example, with a thickness of 100 Å for minimization of the loss of the quantum efficiency, which can then reach 20% (according to Fig. 20).

Another solution of the problem can be the application of the gate grids in the drift gap that are opened by the trigger signal [20, 21] and different schemes of ion feedback suppression [16, 21, 34, 64, 66], for example, the GPD scheme with the photoelectric gate shown in Fig. 6 [66].

Further development of sealed GPDs will be related with the increase in their lifetime, i.e., with the decrease in the photocathode aging rate. The photocathode aging is determined by ion bombardment and interaction with active molecules emitted from the structural elements and formed in the avalanche as a result of plasma-chemical processes. The latter can be avoided if GPD operates with pure noble gases. Another method of extending the photocathode lifetime and increasing GPD gain can be the protection of the photocathodes using the dielectric CsBr and CsI nanofilms mentioned already. Variants of replacement of GEM materials by more inert ones, e.g., silicon or glass [124], are also considered.

4.4. Secondary Processes in GEM-based GPDs

Secondary processes in GPDs are the effects caused by the photon feedback, ion feedback, charging-up of dielectric surfaces by the ion backflow, and photocathode aging under the conditions of gas amplification.

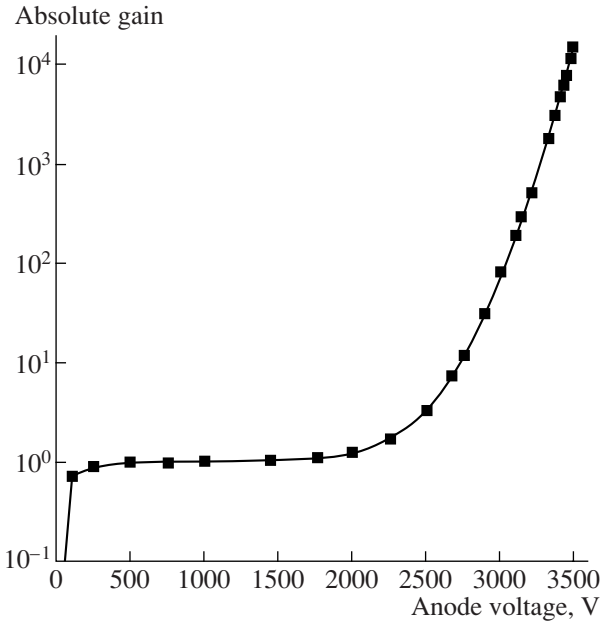

Fig. 42. Gain for GPD with opaque K–Cs–Sb photocathode coated with CsBr film with a thickness of 300 Å in CH_4 in the parallel-plate gap with a thickness of 1 mm as a function of voltage [28].

Their mechanisms were briefly discussed in Section 4.1. Secondary processes play a more important role in gaseous photodetectors than in vacuum photodetectors; in particular, they are the main factor limiting GPD gain and lifetime. In this section, the most characteristic manifestations of secondary processes are considered.

In the case of the GPD with the reflective photocathode deposited on GEM, the photon feedback is completely absent. In the case of the GPD with the semitransparent photocathode, the photon feedback to the photocathode due to avalanche scintillations is efficiently suppressed by the GEM cascade, since the transparency of each GEM is only about 10% [11].

Correspondingly, the photon feedback of this type begins to be manifested only at rather high gains in the form of secondary pulses. In CF_4, secondary pulses caused by the photon feedback occur in particular time intervals for gains higher than 5×10^6 [12] (see Fig. 43). The interval between the pulses, obviously, is equal to the electron drift time from the photocathode to the anode.

In pure noble gases, secondary pulses due to photon feedback usually have an irregular structure [11], since the time of scintillation luminescence in them can be rather large, up to several microseconds [9]. This is related to photon feedback caused by both proportional scintillations in the drift gap and the avalanche scintillations (see Fig. 3).

The ion feedback from the GEM to the photocathode or between the GEM cascades is also manifested in

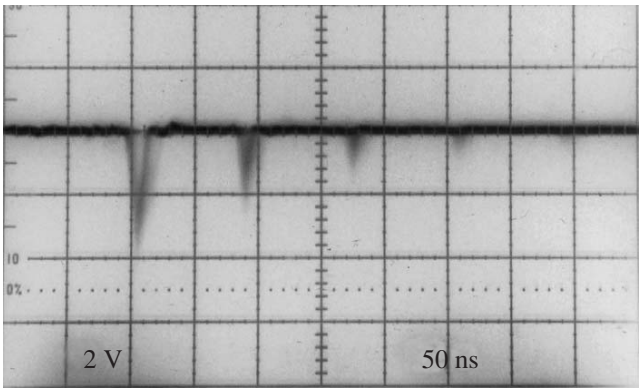

Fig. 43. Photon feedback in three-stage GEM-based GPD with semitransparent CsI photocathode in CF_4 [12]. Anode signal for a gain of 6×10^6 is shown.

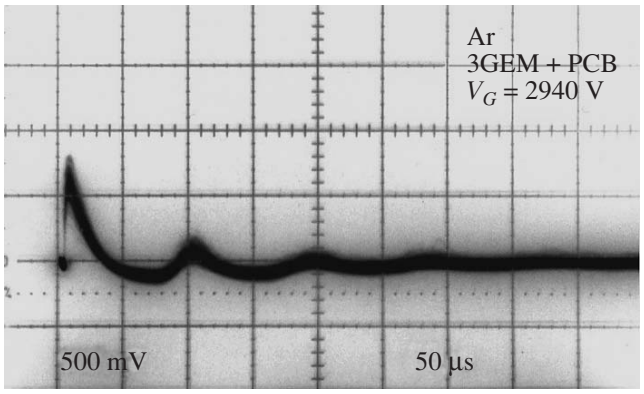

Fig. 44. Ion feedback in three-stage GEM-based GPD with semitransparent CsI photocathode in Ar [11]. Anode signal for a gain of about 10^5 is shown.

the form of the secondary pulses [11, 104, 58]. It is especially characteristic for operation in pure noble gases, since the coefficient of ion-induced electron emission in them is large compared to molecular gases [123]. It can be seen from Fig. 44 that in the GPD with the CsI photocathode, the primary signal in Ar begins to be accompanied by secondary signals for gains of about 10^5. In this case, the interval between the pulses is equal to the ion drift time from the last to the first GEM [11]. In GPDs with photocathodes for the visible range, as was already mentioned, secondary signals due to ion feedback can occur at much lower gains, on the order of 100. It should be noted that the time scales of the photon and the ion feedback differ by three orders of magnitude. Finally, both processes limit the maximum GPD gain.

The key role in the ion feedback is played by ion-induced electron emission from the photocathode or the GEM electrode, which is due to the ion backflow from the avalanche region (Fig. 3) and which is almost instantaneous [123]. There exists another, relatively "slow" effect caused by the ion backflow whose characteristic time is of order of several minutes: the effect of charging-up the dielectric surfaces by ions, which is manifested at large fluxes and gains [11, 104, 105]. This effect is due to the fact that positive ions on the surface of the dielectric, in particular, on the Kapton surface in the GEM or the CsI photocathode hole, have no time for neutralization at large anode current densities, forming a positive surface charge.

In the GEM hole, the positive surface charge creates additional electric field (see Fig. 3), which results in an increase in the gas gain. This was observed, in particular, in GEM operation (without a photocathode) in Ar for anode current densities on the order of 100 pA/mm^2 [105]. On the photocathode, the positive surface charge creates a strong electric field, which can considerably increase the quantum efficiency due to the decreased work function; this phenomenon was considered in Section 2.4. In GPDs, both these phenomena result in the same effect, an increase in the anode signal amplitude. Therefore, it is rather difficult to separate the contributions from these effects.

In the characteristic gain measured in the current mode, the effects of charging-up by ions and the ion feedback are manifested similarly: for high gain values, it grows faster than the exponential function (see Fig. 45). At the same time, unlike the ion feedback, for the ion charging-up the anode signal amplitude depends on time [104] and flux [11]. This is the signature of the effect. This dependence is demonstrated in Fig. 45, which shows the gain characteristics of the GPD in Ar at different fluxes [11]. Judging from the fact that the influence of the flux is already noticeable at anode current

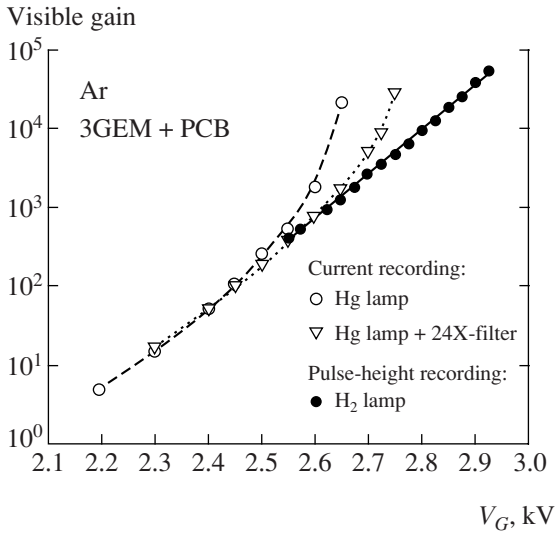

Fig. 45. Effect of charging-up of dielectric surfaces by ion backflow in three-stage GEM-based GPD with semitransparent CsI photocathode in Ar [11]. (Left scale) Gain as a function of the voltage on the divider for different fluxes measured in the counting and the current modes (in the latter case, for two flux values differing by a factor of 24); (right scale) anode current density for the maximum flux.

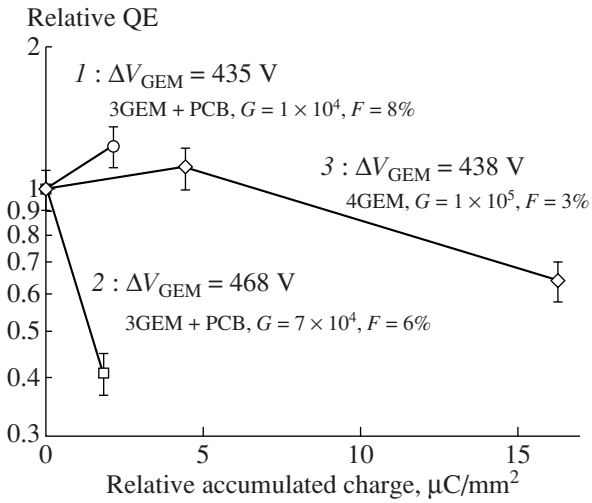

Fig. 46. Aging of sealed GEM-based GPD with semitransparent CsI photocathode in Ar + 5% CH_4 [16]. Relative quantum efficiency of the photocathode as a function of the density of passed anode charge in the configuration with the three-stage GEM (3GEM + PCB) for gains of 10^4 and 7×10^4, and the four-stage GEM (4GEM) for a gain of 10^5 are shown. The values of the voltage on each GEM and the fraction of the ion backflow to the photocathode are also shown.

densities on the order of 10 pA/mm^2, in this case, most probably, the CsI photocathode surface charging-up takes place.

In conclusion to this section, let us mention the photocathode aging effect in sealed GPDs under the conditions of gas gain (photocathode aging in unsealed GPDs based on wire chambers was considered in [6, 21, 28, 69, 82]). Figure 46 shows the dependence of the efficiency of the CsI photocathode on the density of the passed anode charge in the cascade-GEM based sealed GPD [16]. In the configuration with the three-stage GEM, the photocathode efficiency dropped by a factor of two after a charge of 2 μC/mm^2 passed at the anode for a gain on the order of 10^5 in the Ar + 5% CH_4 mixture. This is comparable with the aging rate of both unsealed GPDs with the CsI photocathode [69, 82] and the sealed GPDs with the photocathode for the visible range [21] (see Section 4.3), which testifies to the possible common character of aging mechanisms. The ion backflow to the photocathode probably plays a role in this mechanism. At the same time, it can be seen from Fig. 46 that the photocathode aging is determined by the voltage at the GEM, rather than by the fraction of the ion backflow. This can be explained if it is assumed that the photocathode aging is caused by active molecules and ions whose production rate depends on the electron temperature in the avalanche, i.e., the voltage at the GEM. It follows from the above that the GPD aging rate under the conditions of gas gain can be considerably decreased by increasing the number of GEM cascades [16] or even reduced to zero if operation in pure noble gases is considered.

4.5. GPDs Based on Other Gas Amplification Structures

At present, GEM-based GPDs have been best developed and have shown the best results. At the same time, GPDs based on other gas amplification structures, such as microhole and strip plates [21], capillary plates [54, 122], microchannel plates [125], thick GEMs [56], thick GEMs with resistive electrodes [57], and Micromegas [126] continue to be studied. The most complete description of the state of GPDs with other amplification structures can be found in review [124].

CONCLUSIONS

In this review, the results of research and development of gaseous photodetectors with solid photocathodes (GPDs) were presented. The principles of operation of GPDs and their basic characteristics were considered. GPDs based on gas electron multipliers (GEMs), including sealed GPDs and cryogenic two-phase avalanche detectors with the CsI photocathode, were considered in detail. Efficient photocathodes for the ultraviolet and the visible ranges were described in relation with their application in GPDs. A separate chapter was devoted to protective dielectric nanofilms on photocathodes. The most interesting problems of the physics of gaseous photodetectors and photocathodes, such as photoelectron backscattering in gas, enhancement of photoelectron emission in an electric field, photoelectron transport through nanofilms, the protective properties of nanofilms, and photon and ion feedback, were considered.

The remarkable properties of PGDs make them attractive for applications in high energy physics, astrophysics, and medical imaging. In particular, the high efficiency and high gain of GPDs with CsI photocathodes provided the possibility of successful application in RICH detectors. The capability of operation of GEM-based GPDs in pure noble gases allowed the development of cryogenic two-phase avalanche detectors with CsI photocathodes, which are used in experiments on detection of coherent neutrino scattering off nuclei, dark matter detection, and in positron emission tomography.

GPDs with photocathodes for the visible range are actively being developed. Impressive results concerning their operation in the sealed configuration and with photocathodes protected by dielectric nanofilms were obtained. Further progress in this field will obviously depend on development in the technology of production of these devices.

ACKNOWLEDGMENTS

We thank A.E. Bondar', D.V. Pavlyuchenko, Yu.A. Tikhonov, and L.I. Shekhtman for fruitful discussions.

REFERENCES

1. J. Seguinot and T. Ypsilantis, "A Historical Review of Ring Imaging Cherenkov Counters," Nucl. Instrum. Methods Phys. Res. A **343**, 1 (1994).
2. A. Breskin, T. Boutboul, A. Buzulutskov, et al., "Advances in Gas Avalanche Photomultipliers," Nucl. Instrum. Methods Phys. Res. A **442**, 58 (2000).
3. E. N. Pavlova, *Gas Discharge Photon Counters* (Len. Gos. Univ, Leningrad, 1966) [in Russian].
4. J. Seguinot and T. Ypsilantis, "Photo-Ionization and Cherenkov Ring Imaging," Nucl. Instrum. Methods Phys. Res. **142**, 377 (1977).
5. G. Bogomolov, Y. Dubrovski, and V. Peskov, "Multiwire Gas Counters for Coordinate Measurements in Ultraviolet Region," Instr. Exp. Tech. **21**, 779 (1978).
6. A. Breskin, "CsI UV Photocathodes: History and Mystery," Nucl. Instrum. Methods Phys. Res. A **371**, 116 (1996).
7. G. Charpak, W. Dominik, F. Sauli, and S. Majewski, "The Gas Photodiode As a Possible Large-Area Photon Detector," IEEE Trans. Nucl. Sci. **NS-30**, 134 (1983).
8. E. M. Gushchin, S. V. Somov, and M. K. Timofeev, "Investigation of Gas Discharge Impulse Image Intensifiers," Prib. Tekh. Eksp., No. 4, 95 (1996).
9. A. S. Barabash and A. I. Bolozdynya, "Liquid Ionization Detectors" (Energoatomizdat, Moscow, 1993) [in Russian].
10. A. Di Mauro, "Recent CsI-RICH Developments," Nucl. Instrum. Methods Phys. Res. A **525**, 173 (2004).
11. A. Buzulutskov, A. Breskin, R. Chechik, et al., "The GEM Photomultiplier Operated with Noble Gas Mixtures," Nucl. Instrum. Methods Phys. Res. A **443**, 164 (2000).
12. A. Breskin, A. Buzulutskov, and R. Chechik, "GEM Photomultiplier Operation in CF_4," Nucl. Instrum. Methods Phys. Res. A **483**, 670 (2002).
13. D. Mörmann, A. Breskin, R. Chechik, and C. Shalem, "Operation Principles and Properties of the Multi-GEM Gaseous Photomultiplier with Reflective Photocathode," Nucl. Instrum. Methods Phys. Res. A **530**, 258 (2004).
14. T. Meinschad, L. Ropelewski, and F. Sauli, "GEM-Based Photon Detector for RICH Applications," Nucl. Instrum. Methods Phys. Res. A **535**, 324 (2004).
15. A. Breskin, A. Buzulutskov, R. Chechik, et al., "Sealed Gas UV-Photon Detector with a Multi-GEM Multiplier," IEEE Trans. Nucl. Sci. **48**, 417 (2001).
16. A. Breskin, A. Buzulutskov, R. Chechik, et al., "Sealed GEM Photomultiplier with a CsI Photocathode: Ion Feedback and Ageing," Nucl. Instrum. Methods Phys. Res. A **478**, 225 (2002).
17. E. Shefer, A. Breskin, A. Buzulutskov, et al., "Laboratory Production of Efficient Alkali-Antimonide Photocathodes," Nucl. Instrum. Methods Phys. Res. A **411**, 383 (1998).
18. R. Chechik, M. Balcerzyk, A. Breskin, et al., "Progress in GEM-Based Gaseous Photomultipliers," Nucl. Instrum. Methods Phys. Res. A **502**, 195 (2003).
19. D. Mörmann, M. Balcerzyk, A. Breskin, et al., "GEM-Based Gaseous Photomultipliers for UV and Visible Photon Imaging," Nucl. Instrum. Methods Phys. Res. A **504**, 93 (2003).
20. M. Balcerzyk, D. Mörmann, A. Breskin, et al., "Methods of Preparation and Performance of Sealed Gas Photomultipliers for Visible Light," IEEE Trans. Nucl. Sci. **50**, 847 (2003).
21. A. Breskin, D. Mörmann, A. Lyashenko, et al., "Ion-Induced Effects in GEM and GEM/MHSP Gaseous Photomultipliers for the UV and the Visible Spectral Range," Nucl. Instrum. Methods Phys. Res. A **553**, 46 (2005).
22. A. Buzulutskov, A. Breskin, R. Chechik, and J. Vavra, "Study of Photocathode Protection with Thin Dielectric Films," Nucl. Instrum. Methods Phys. Res. A **371**, 147 (1996).
23. A. Buzulutskov, A. Breskin, and R. Chechik, "Photoemission through Thin Dielectric Coating Films," J. of Appl. Phys. **81**, 466 (1997).
24. A. Breskin, A. Buzulutskov, R. Chechik, et al., "Evidence for Thin-Film Protection of Visible Photocathodes," Appl. Phys. Lett. **69**, 1008 (1996).
25. A. Buzulutskov, A. Breskin, R. Chechik, et al., "Protection of Cesium-Antimony Photocathodes," Nucl. Instrum. Methods Phys. Res. A **387**, 176 (1997).
26. A. Buzulutskov, E. Shefer, A. Breskin, et al., "The Protection of K–Cs–Sb Photocathodes with CsBr Films," Nucl. Instrum. Methods Phys. Res. A **400**, 173 (1997).
27. E. Shefer, A. Breskin, A. Buzulutskov, et al., "Composite Photocathodes for Visible Photon Imaging with Gaseous Photomultipliers," Nucl. Instrum. Methods Phys. Res. A **419**, 612 (1998).
28. E. Shefer, A. Breskin, R. Chechik, et al., "Coated Photocathodes for Visible Photon Imaging with Gaseous Photomultipliers," Nucl. Instrum. Methods Phys. Res. A **433**, 502 (1999).
29. A. Breskin, A. Buzulutskov, E. Shefer, et al., "Removable Organic Protective Coating for Alkali-Antimonide Photocathodes," Nucl. Instrum. Methods Phys. Res. A **413**, 275 (1998).
30. J. H. He and T. A. Kunitake, "Are Ceramic Nanofilms a Soft Matter?," Soft Matter **2**, 119 (2006).
31. F. Sauli, "Principles of Operation of Multiwire Proportional and Drift Chambers," in *Experimental Techniques in High Energy Physics*, Ed. by T. Ferbel (Addison-Wesley, Reading, MA, 1987); Preprint CERN 77-09 (1977).
32. F. Sauli, "A New Concept for Electron Amplification in Gas Detectors," Nucl. Instrum. Methods Phys. Res. A **386**, 531 (1997).
33. F. Sauli, "Progress with the Gas Electron Multiplier," Nucl. Instrum. Methods Phys. Res. A **522**, 93 (2004).
34. A. F. Buzulutskov, "Radiation Detectors Based on Gas Electron Multipliers," Prib. Tekh. Eksp., No. 3, 5 (2007); Instr. Exp. Tech. **50**, 287–310 (2007).
35. Z. Fraenkel, A. Kozlov, M. Naglis, et al., "A Hadron Blind Detector for the PHENIX Experiment at RHIC," Nucl. Instrum. Methods Phys. Res. A **546**, 466 (2005).
36. A. Kozlov, I. Ravinovich, L. Shekhtman, et al., "Development of a Triple GEM UV-Photon Detector Operated in Pure CF_4 for the PHENIX Experiment," Nucl. Instrum. Methods Phys. Res. A **523**, 344 (2004).

37. A. Milov, W. Anderson, B. Azmoun, et al., "Construction and Expected Performance of the Hadron Blind Detector for the PHENIX Experiment at RHIC," http://arxiv.org/physics/0701273 (2007).
38. A. Buzulutskov, A. Bondar, L. Shekhtman, et al., "First Results from Cryogenic Avalanche Detectors Based on Gas Electron Multipliers," IEEE Trans. Nucl. Sci. **50**, 2491 (2003).
39. A. Bondar, A. Buzulutskov, A. Grebenuk, et al., "First Results of the Two-Phase Argon Avalanche Detector Performance with CsI Photocathode," Nucl. Instrum. Methods Phys. Res. A **581**, 241 (2007); http://arxiv.org/physics/0702237 (2007).
40. C. Hagmann and A. Bernstein, "Two-Phase Emission Detector for Measuring Coherent Neutrino-Nucleus Scattering," IEEE Trans. Nucl. Sci. **51**, 2151 (2004).
41. D. Yu. Akimov, "Experimental Methods for Particle Dark Matter Detection," Prib. Tekh. Eksp., No. 5, 6 (2001) [Instr. Exp. Tech. **44**, 575–617 (2001).
42. A. Rubbia, "ArDM: a Ton-Scale Liquid Argon Experiment for Direct Detection of Dark Matter in the Universe," http://arxiv.org/hep-ph/0510320.
43. M. Chen and A. Bolozdynya, "Radiation Detection and Tomography," US patent 5 665 971 (1997).
44. A. Buzulutskov et al., "Gas Electron Multiplier-Based Detectors Operated with Dense Noble Gases for Astroparticle, Medical and Neutron Imaging," Proposal for CRDF Grant RP1-2550-NO-03 (2003); in *Proc. of Intern. Symp. on Development of Detectors for Particle, Astro-Particle and Synchrotron Radiation Experiments, SLAC, Stanford, CA, USA, April 3–6, 2006*; http://www-conf.slac.stanford.edu/snic/.
45. A. Buzulutskov, A. Breskin, and R. Chechik, "Heat Enhancement of the Photoyield from CsI, NaI, and CuI Photocathodes," Nucl. Instrum. Methods Phys. Res. A **366**, 410 (1995).
46. A. Breskin, A. Buzulutskov, R. Chechik, et al., "Electric Field Effects on CsI Quantum Efficiency in Gas Media," Nucl. Instrum. Methods Phys. Res. A **344**, 537 (1994).
47. A. Breskin, A. Buzulutskov, R. Chechik, et al., "Field-Dependent Photoelectron Extraction from CsI in Different Gases," Nucl. Instrum. Methods Phys. Res. A **367**, 342 (1995).
48. A. Di Mauro, E. Nappi, F. Posa, et al., "Photoelectron Backscattering Effects in Photoemission from CsI into Gas Media," Nucl. Instrum. Methods Phys. Res. A **371**, 137 (1996).
49. J. Almeida, A. Amadon, P. Besson, et al., "Review of the Development of Cesium Iodide Photocathodes for Application to Large RICH Detectors," Nucl. Instrum. Methods Phys. Res. A **367**, 332 (1995).
50. J. Almeida, A. Braem, A. Breskin, et al., "Microanalysis Surface Studies and Photoemission Properties of CsI Photocathodes," Nucl. Instrum. Methods Phys. Res. A **367**, 337 (1995).
51. D. Cozza, G. De Cataldo, D. Dell'Olio, et al., "The CSI-Based RICH Detector Array for the Identification of High Momentum Particles in ALICE," Nucl. Instrum. Methods Phys. Res. A **502**, 101 (2003).
52. K. Zeitelhack, A. Elhardt, J. Friese, et al., "The HADES RICH Detector: For the HADES Collaboration," Nucl. Instrum. Methods Phys. Res. A **433**, 201 (1999).
53. H. Sakuray, T. Tamura, S. Gunji, and M. Noma, "A New Type of Proportional Counter Using a Capillary Plate," Nucl. Instrum. Methods Phys. Res. A **374**, 341 (1996).
54. V. Peskov, E. Silin, T. Sokolova, and I. Rodionov, "First Attempts to Combine Capillary Tubes with Photocathodes," Nucl. Instrum. Methods Phys. Res. A **433**, 492 (1999).
55. J. M. Maia, J. F. C. A. Veloso, J. M. F. dos Santos, et al., "Advances in the Micro-Hole & Strip Plate Gaseous Detector," Nucl. Instrum. Methods Phys. Res. A **504**, 364 (2003).
56. C. Shalem, R. Chechik, A. Breskin, and K. Michaeli, "Advances in Thick GEM-Like Gaseous Electron Multipliers. Part I: Atmospheric Pressure Operation," Nucl. Instrum. Methods Phys. Res. A **558**, 475 (2006).
57. R. Oliveira, V. Peskov, F. Pietropaolo, and P. Picchi, "First Tests of Thick GEMs with Electrodes Made of a Resistive Kapton," Nucl. Instrum. Methods Phys. Res. A **576**, 362 (2006).
58. A. Buzulutskov, "Physics of Multi-GEM Structures," Nucl. Instrum. Methods Phys. Res. A **494**, 148 (2002).
59. A. Bondar, A. Buzulutskov, L. Shekhtman, et al., "Cryogenic Avalanche Detectors Based on Gas Electron Multipliers," Nucl. Instrum. Methods Phys. Res. A **524**, 130 (2004).
60. A. Buzulutskov, J. Dodd, R. Galea, et al., "GEM Operation in Helium and Neon at Low Temperatures," Nucl. Instrum. Methods Phys. Res. A **548**, 487 (2005).
61. A. Bondar, A. Buzulutskov, A. Grebenuk, et al., "Two-Phase Argon and Xenon Avalanche Detectors Based on Gas Electron Multipliers," Nucl. Instrum. Methods Phys. Res. A **556**, 273 (2006).
62. A. Bondar, A. Buzulutskov, A. Grebenuk, et al., "A Two-Phase Argon Avalanche Detector Operated in a Single Electron Counting Mode," Nucl. Instrum. Methods Phys. Res. A **574**, 493 (2007).
63. S. Bachmann, A. Bressan, L. Ropelewski, et al., "Charge Amplification and Transfer Processes in the Gas Electron Multiplier," Nucl. Instrum. Methods Phys. Res. A **438**, 376 (1999).
64. A. Bondar, A. Buzulutskov, L. Shekhtman, and A. Vasiljev, "Study of Ion Feedback in Multi-GEM Structures," Nucl. Instrum. Methods Phys. Res. A **496**, 325 (2003).
65. F. Sauli, S. Kappler, and L. Ropelewski, "Electron Collection and Ion Feedback in GEM-Based Detectors," IEEE Trans. Nucl. Sci. **50**, 803 (2003).
66. A. Buzulutskov and A. Bondar, "Electric and Photoelectric Gates for Ion Feedback Suppression in Multi-GEM Structures," J. of Instrumentation **1**, 08006 (2006).
67. J. F. C. A. Veloso, F. D. Amaro, J. M. F. dos Santos, et al., "The Photon-Assisted Cascaded Electron Multiplier: A Concept for Potential Avalanche-Ion Blocking," J. of Instrumentation **1**, 08003 (2006).
68. A. H. Sommer, *Photoemissive Materials* (Krieger, Huntington, 1980).
69. B. K. Singh, E. Shefer, A. Breskin, et al., "CsBr and CsI UV Photocathodes: New Results on Quantum Efficiency and Aging," Nucl. Instrum. Methods Phys. Res. A **454**, 364 (2000).

70. A. Laikhtman, Y. Avigal, R. Kalish, et al., "Surface Quality and Composition Dependence of Absolute Quantum Photoyield of CVD Diamond Films," Diamonds and Related Materials **8**, 725 (1999).
71. P. Fonte, T. Francke, N. Pavlopoulos, et al., "Novel Single Photon Detectors for UV Imaging," Nucl. Instrum. Methods Phys. Res. A **553**, 30 (2005).
72. E. A. Taft and H. R. Philipp, J. Phys. Chem. Solids **3**, 1 (1957).
73. G. F. Carruthers, Appl. Opt. **14**, 1667 (1975).
74. V. Dangendorf, A. Breskin, R. Chechik, and H. Schmidt-Böcking, "A Gas Filled UV-Photon Detector with CsI Photocathode for the Detection of Xe Light," Nucl. Instrum. Methods Phys. Res. A **289**, 322 (1990).
75. J. Seguinot, G. Charpak, Y. Giomataris, et al., "Reflective UV Photocathodes with Gas-Phase Electron Extraction: Solid, Liquid, and Absorbed Thin Films," Nucl. Instrum. Methods Phys. Res. A **297**, 133 (1990).
76. C. Lu and K. T. McDonald, "Properties of Reflective and Semitransparent CsI Photocathodes," Nucl. Instrum. Methods Phys. Res. A **343**, 135 (1994).
77. A. Breskin, R. Chechik, D. Vartsky, et al., "A Correction to the Quantum Efficiency of CsI and Other Photocathodes Due to the Recalibration of the Reference Photomultipliers," Nucl. Instrum. Methods Phys. Res. A **343**, 159 (1994).
78. D. F. Anderson, S. Kwan, V. Peskov, and B. Hoeneisen, Nucl. Instrum. Methods Phys. Res. A **323**, 626 (1992).
79. A. Breskin, A. Buzulutskov, and R. Chechik, "New Ideas in CsI-Based Photon Detectors: Wire Photomultipliers and Protection of Photocathodes," IEEE Trans. Nucl. Sci. **42**, 298 (1995).
80. H. Hoedlmoser, A. Braem, G. De Cataldo, et al., "Production Technique and Quality Evaluation of CsI Photocathodes for the ALICE/HMIPD Detector," Nucl. Instrum. Methods Phys. Res. A **566**, 338 (2006).
81. A. Buzulutskov, A. Breskin, and R. Chechik, "Field Enhancement of Photoelectric and Secondary Electron Emission from CsI," J. of Appl. Phys. **77**, 2138 (1995).
82. J. Vavra, A. Breskin, A. Buzulutskov, et al., "Study of CsI Photocathodes: Volume Resistivity and Ageing," Nucl. Instrum. Methods Phys. Res. A **387**, 154 (1997).
83. E. Aprile, A. Bolotnikov, D. Chen, et al., "Electron Extraction from a CsI Photocathode into Condensed Xe, Kr, and Ar," Nucl. Instrum. Methods Phys. Res. A **343**, 129 (1994).
84. L. Periale, V. Peskov, C. Iacobaeus, et al., "Photosensitive Gaseous Detectors for Cryogenic Temperature Applications," Nucl. Instrum. Methods Phys. Res. A **573**, 302 (2007).
85. A. S. Tremsin and O. H. W. Siegmund, "Heat Enhancement of Radiation Resistivity of Evaporated CsI, KI, and KBr Photocathodes," Nucl. Instrum. Methods Phys. Res. A **442**, 337 (2000).
86. G. Charpak, D. Lemenovski, V. Peskov, and Scigocki, Nucl. Instrum. Methods Phys. Res. A **310**, 128 (1991).
87. L. B. Leob, *Basic Processes of Gaseous Electronics* (Univ. of California, Berkeley, 1955), p. 601.
88. J. Escada, T. H. V. T. Dias, P. J. B. M. Rachinhas, et al., "A Monte Carlo Study of Backscattering Effects in the Photoelectron Emission from CsI into CH_4 and Ar–CH_4 Mixtures," J. of Instrumentation **2**, 08001 (2007).
89. A. Buzulutskov, L. Shekhtman, A. Bressan, et al., "GEM Operation in Pure Noble Gases and the Avalanche Confinement," Nucl. Instrum. Methods Phys. Res. A **433**, 471 (1999).
90. A. Buzulutskov, A. Breskin, R. Chechik, and D. Vartsky, "Field Enhanced Response of a CsI Photocathode to BaF_2 and $KMgF_3$ Scintillation," Nucl. Instrum. Methods Phys. Res. A **350**, 406 (1994).
91. A. F. Buzulutskov, L. K. Turchanovich, and V. G. Vasilchenko, "Coupling of a $KMgF_3$ Scintillator to a Wire Chamber Filled with Triethylamine," Nucl. Instrum. Methods Phys. Res. A **281**, 99 (1989).
92. S. Majewski and K. Zorn, *Instrumentation in High Energy Physics*, Ed. by F. Sauli (World Scientific, Singapore, 1992).
93. G. Charpak, I. Gaudean, Y. Giomataris, et al., Nucl. Instrum. Methods Phys. Res. A **333**, 391 (1993).
94. T. Boutboul, A. Akkerman, A. Gibrekhterman, et al., "An Improved Model for Ultraviolet- and X-ray-Induced Electron Emission from CsI," J. of Appl. Phys. **86**, 5841 (1999).
95. S. Giunji, V. Peskov, H. Sakurai, et al., "Glass Capillary Tubes as a High Granularity Gaseous Detector of Photons and Charged Particles," Nucl. Instrum. Methods Phys. Res. A **477**, 8 (2002).
96. R. Enomoto, T. Sumiyoshi, and Y. Fujita, "Test of Various Photocathodes," Nucl. Instrum. Methods Phys. Res. A **343**, 117 (1994).
97. V. Peskov, A. Borovik-Romanov, T. Sokolova, and E. Silin, "Gaseous Detectors of Ultraviolet and Visible Photons," Nucl. Instrum. Methods Phys. Res. A **353**, 184 (1994).
98. E. Shefer, A. Breskin, T. Boutboul, et al., "Photoelectron Transport in CsI and CsBr Coating Films of Alkali Antimonide and CsI Photocathodes," J. Appl. Phys. **92**, 4758 (2002).
99. A. Buzulutskov, A. Breskin, E. Shefer, et al., "Organic Protective Coatings for Alkali-Antimonide Photocathodes," in *New Detectors*, Ed. by C. Williams and T. Ypsilantis (World Sci., Singapore, 1999), pp. 195–202.
100. T. Boutboul, A. Akkerman, A. Breskin, and R. Chechik, "Escape Length of Ultraviolet Induced Photoelectrons in Alkali Iodide and CsBr Evaporated Films: Measurements and Modeling," J. of Appl. Phys **84**, 2890 (1998).
101. B. E. Evans, L. W. Swanson, and A. E. Bell, Surf. Sci. **11**, 1 (1968).
102. A. Buzulutskov, A. Breskin, and R. Chechik, "Photoemission from CsI/LiF and CsI/NaF Films Enhanced by Exposure to Water Vapor," Nucl. Instrum. Methods Phys. Res. A **372**, 572 (1996).
103. I. M. Yamazaki, L. P. Geraldo, and R. Paterson, "Characterization of Polycarbonate Nuclear Track-Etched Membranes by Means of the Gas Permeation Method," Nucl. Instrum. Methods Phys. Res. A **418**, 491 (1998).
104. A. Buzulutskov, A. Breskin, R. Chechik, et al., "Further Studies of the GEM Photomultiplier," Nucl. Instrum. Methods Phys. Res. A **442**, 68 (2000).

105. A. Bressan, A. Buzulutskov, L. Ropelewski, et al., "High Gain Operation of GEM in Pure Argon," Nucl. Instrum. Methods Phys. Res. A **423**, 119 (1999).

106. S. Bachmann, A. Bressan, B. Ketzer, et al., "Performance of GEM Detectors in High Intensity Particle Beams," Nucl. Instrum. Methods Phys. Res. A **470**, 548 (2001).

107. S. Bachmann, A. Bressan, M. Capeans, et al., "Discharge Studies and Prevention in the Gas Electron Multiplier (GEM)," Nucl. Instrum. Methods Phys. Res. A **479**, 294 (2002).

108. C. Richter, A. Breskin, R. Chechik, et al., "On the Efficient Electron Transfer through GEM," Nucl. Instrum. Methods Phys. Res. **478**, 538 (2002).

109. D. Mörmann, A. Breskin, R. Chechik, and D. Bloch, "Evaluation and Reduction of Ion Back-Flow in Multi-GEM Detectors," Nucl. Instrum. Methods Phys. Res. A **516**, 315 (2004).

110. A. Bondar, A. Buzulutskov, D. Pavluchenko, et al., "Further Studies of GEM Performance at Cryogenic Temperatures," Nucl. Instrum. Methods Phys. Res. A **535**, 299 (2004).

111. A. Bondar, A. Buzulutskov, D. Pavluchenko, et al., "Further Studies of Two-Phase Krypton Detectors Based on Gas Electron Multipliers," Nucl. Instrum. Methods Phys. Res. A **548**, 439 (2005).

112. R. Galea, J. Dodd, Y. Ju, et al., "Gas Purity Effect on GEM Performance in He and Ne at Low Temperatures," IEEE Trans. Nucl. Sci. **53**, 2260 (2006).

113. F. Sauli, "Principles of Operation of Multiwire Proportional and Drift Chambers," in *Experimental Techniques in High Energy Physics*, Ed. by T. Ferbel (Addison-Wesley, Reading, MA, 1987); Preprint CERN 77-09 (1977).

114. A. Bondar, A. Buzulutskov, and L. Shekhtman, "High Pressure Operation of the Triple-GEM Detector in Pure Ne, Ar, and Xe," Nucl. Instrum. Methods Phys. Res. A **481**, 200 (2002).

115. A. Bondar, A. Buzulutskov, L. Shekhtman, et al., "Triple GEM Operation in Compressed He and Kr," Nucl. Instrum. Methods Phys. Res. A **493**, 8 (2002).

116. V. Aulchenko, A. Bondar, A. Buzulutskov, et al., "Further Studies of GEM Performance in Dense Noble Gases," Nucl. Instrum. Methods Phys. Res. A **513**, 256 (2003).

117. A. Bondar, A. Buzulutskov, L. Shekhtman, and A. Vasiljev, "Triple-GEM Performance in He-Based Mixtures," http://arxiv.org/physics/0610059; in *Proc. of Intern. Conf. on Linear Colliders, Paris, April 19–23, 2004*.

118. B. Sitar, G. I. Merson, V. A. Chechin, and Yu. A. Budagov, *Ionization Measurements* (Springer, Berlin, 1993).

119. R. Bellazzini, G. Spandre, A. Brez, et al., "Imaging with the Invisible Light," http://arxiv.org/physics/0703176 (2007).

120. G. P. Guedes, A. Breskin, R. Chechik, et al., "Two-Dimensional GEM Imaging Detector with Delay-Line Readout," Nucl. Instrum. Methods Phys. Res. A **513**, 473 (2003).

121. J. M. Maia, A. Breskin, D. Mörmann, et al., "Progress in MHSP Electron Multiplier Operation," IEEE Trans. Nucl. Sci. **51**, 1503 (2004).

122. V. Biteman, S. Guinji, V. Peskov, et al., "Position Sensitive Gaseous Photomultipliers," Nucl. Instrum. Methods Phys. Res. A **471**, 205 (2001).

123. Yu. P. Raizer, *Gas Discharge Physics* (Nauka, Moscow, 1987; Springer-Verlag, Berlin, 1991).

124. A. Breskin, "Advances in Gaseous Photomultipliers," in *Proc. of 4th Intern. Conf. on New Developments in Photodetection, Beaune, France, June 19–24, 2005*, http://beaune.in2p3.fr.

125. J. Vavra and T. Sumiyoshi, "Ion Feedback Suppression Using Inclined MCP Holes in a "single-MCP + micromegas + pads" Detector," Nucl. Instrum. Methods Phys. Res. A **553**, 76 (2005).

126. G. Charpak, J. Derre, Y. Giomataris, and P. Rebourgeard, "Micromegas, a Multipurpose Gaseous Detector," Nucl. Instrum. Methods Phys. Res. A **478**, 26 (2002).